

UDK 528, 504.5.06, 55

DOI: <http://doi.org/10.17721/1728-2713.110.12>

Arif HUSEYNOV, Master of Arts (Earth Sciences)

ORCID ID: 0000-0002-9941-3221

e-mail: huseynovarif85@gmail.com

Institute of Oil and Gas Ministry of Science and Education of the Republic of Azerbaijan, Baku, Azerbaijan

Viktor NESTEROVSKIY, DSc (Geol.), Prof.

ORCID ID: 0000-0002-7065-8962

e-mail: v.nesterovski@ukr.net

Taras Shevchenko National University of Kyiv, Kyiv, Ukraine

Ayten HUSEYNOVA, PhD (Earth Sciences)

ORCID ID: 0000-0002-1932-4289

e-mail: aytenhuseynova@anas.az

Presidium of the National Academy of Sciences of Azerbaijan, Baku, Azerbaijan

FIRST EXPERIENCE IN USING SATELLITE DATA FOR MONITORING THE HYDRO-FLUID REGIME OF LOKBATAN VOLCANO IN THE ASSESSMENT OF SEISMIC EVENT RISKS IN THE REGION

(Представлено членом редакційної колегії д-ром геол. наук, ст. наук. спієроб. О.Л. Шевченком та д-ром геогр. наук, проф. Д.О. Ляшенко)

Background. Mud volcanoes are unique natural structures affecting the environment by continuous emissions of gas-liquid fluids, mud breccia and mudflows. Despite extensive research and a substantial dataset on mud volcanism, the understanding of the fluid dynamics and hydrogeological processes associated with these systems remains a subject of ongoing debate. Globally, there are more than 2,500 mud volcanoes distributed across 42 countries (Aliyev et al., 2015), highlighting their widespread occurrence.

Azerbaijan represents a unique region for the study of contemporary mud volcanism, hosting more than 350 mud volcanoes within a relatively small territory. Among them, the Lokbatan mud volcano is the most active, with 28 recorded eruptions. In this context, a comprehensive approach to studying the activity of mud volcanoes, including satellite monitoring, is highly relevant.

Methods. The study employed remote sensing techniques to analyze the hydro-fluid regime of the Lokbatan mud volcano. Specifically, satellite imagery was used to calculate a moisture index for the volcano field. For the first time, this index was remotely measured, enabling assessment of surface moisture dynamics as a proxy for fluid migration and subsurface activity.

Results. The satellite-derived moisture index showed clear correlations with mud volcanic activity. Observations indicate that variations in the moisture index correspond to shifts in the fluid regime of the volcano, reflecting possible underground fluid migration or pressure changes prior to eruptions.

Conclusions. The study demonstrates the potential of satellite-based monitoring in assessing the hydro-fluid regime of active mud volcanoes. The approach provides an effective, low-cost alternative to field-based observations and can support early warning systems for seismic or eruptive events. These findings contribute to the development of preventive strategies for managing geological hazards in seismically active regions.

Keywords: Mud volcano, satellite images, fluids, NDWI, monitoring.

Background

In the modern world, an integrated approach to solving challenges in Earth sciences is highly demanded and widely applicable. Today, satellite imagery, drone surveys, and other remote sensing technologies are increasingly used for data collection, analysis, and interpretation. By using modern technologies, the time and effort required to obtain such data are significantly reduced, making previously inaccessible research sites available without excessive risks or additional costs. In this study, satellite monitoring was applied for the first time to measure the moisture index at Lokbatan mud volcano.

The object of the research is the Lokbatan mud volcano, located 17 km southwest of Baku (Fig. 1). This choice is justified by the specific geological structure of the volcano, its eruption activity, proximity to the urban agglomeration, and spatial connection with the oil field.

Analysis of Previous Studies

Mud volcanoes of the Absheron Peninsula in Azerbaijan have a long history of study. The main research efforts have been conducted in connection with oil and gas exploration. Significant contributions in this field have been made by F. Dadashev, A. Yakubov, Ad. Aliyev, I. Guliyev, A. Feyzullayev, D. Guseynov, A. Mazzini, M. Schmidt, G. Etiope, and others. Their publications

have examined in detail the morphology and genesis of mud volcanoes, the relationship between mud volcanism and hydrocarbon occurrences, the estimation of combustible gas volumes released during eruptions, and the physical-mathematical modeling of mud volcanoes.

In recent years, some researchers have begun to consider mud volcanoes as one of the major natural sources of greenhouse gas emissions into the atmosphere. Accordingly, several studies have focused on the role of mud volcanism in climate change processes. It is also worth noting that one of the modern and promising directions today is the use of satellite technologies, particularly data from the Sentinel mission, for remote monitoring of mud volcano activity. For example, NDWI was effectively used to analyze the spread of the Sidoarjo mudflow (Indonesia) (Wicaksono and Isa, 2022). Additionally, a number of monographs and color atlases have been published aimed at popularizing knowledge about mud volcanoes and promoting geological tourism in the country (Aliyev et al., 2015; Aliyev, Guliyev, & Rahmanov, 2019; hnyukov, 2006).

Objective of the Study

The aim of this study is to explore the potential of using satellite data for monitoring mud volcanic activity on the Absheron Peninsula of Azerbaijan, using the most active volcano, Lokbatan, as a case study.

© Huseynov Arif, Nesterovskiy Viktor, Huseynova Ayten, 2025

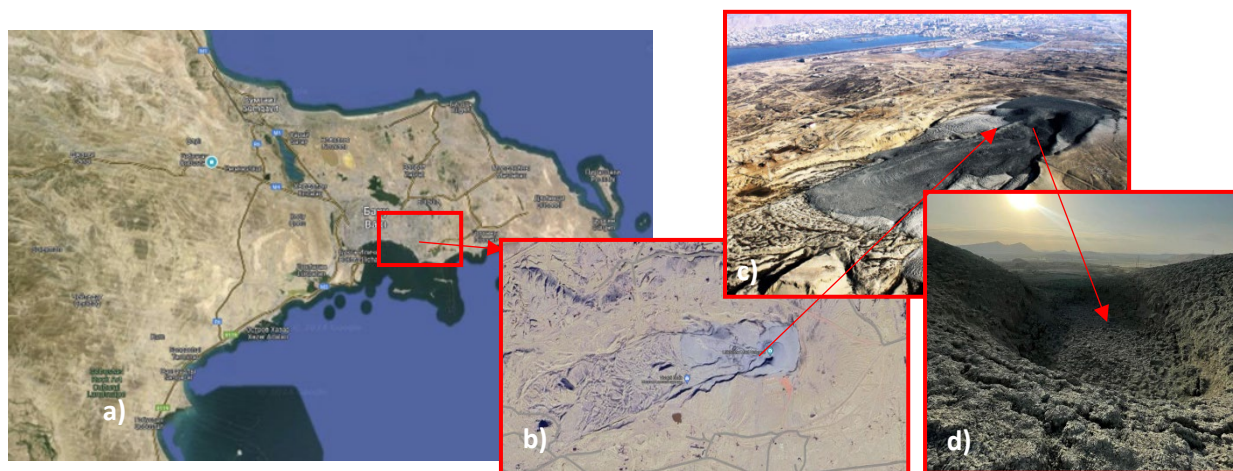


Fig. 1. (a, b) Location of the Lokbatan mud volcano (a, b)? (source: Google Maps); (c) aerial photograph of the general view (c) ? (photo by A.R. Huseynov); (d) view of the crater field (d)? (photo by V. Shukyurov)

Methods

To study the fluid regime of the Lokbatan volcano, satellite monitoring was applied using the Normalized Difference Water Index (NDWI) based on Sentinel-2 satellite data. The methodology consisted of several stages: collection and calibration of satellite images, calculation of NDWI for assessing water bodies and soil moisture, analysis of time series from 2017 to 2023, mapping of changes (using Google Earth), and data interpretation. NDWI values greater than 0 indicate wet soil, while values below 0 represent dry areas. The resulting data were presented in KMZ format and used for analyzing the dynamics of fluid processes on the volcano. The extracted NDWI values for the volcano were plotted on a graph, which allowed for the visualization of changes in the water regime.

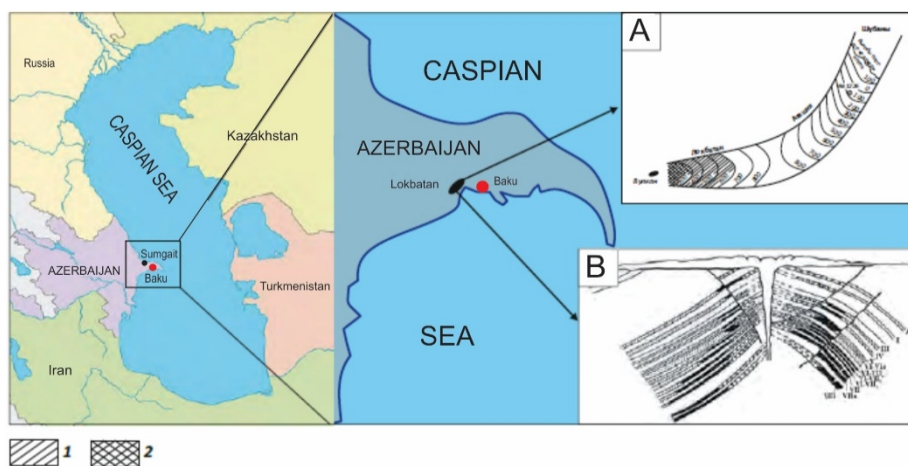
Main Material Presentation and Its Analysis

The Lokbatan mud volcano in relief represents a small dome with two peaks and an absolute elevation of 86 meters. The base of the mud volcano structure measures

2.5 km by 2.3 km, covering an area of 5.75 km². Structurally, the mud volcano is situated on the crest of an asymmetrical brachyanticline of latitudinal orientation, which extends and connects with the Akhtarma-Puta and Gushkhana brachyanticlines, forming a unified Lokbatan–Putā–Gushkhana anticline zone. Besides Lokbatan, the mud volcanoes of Akhtarma-Puta and Gushkhana are also located here (Yakubov, Kastyulin, & Dzhabadov, 1976a; Yakubov, Aliyev, & Rakhmanov, 1976b).

In 1927, the Lokbatan hydrocarbon field was discovered near the mud volcano, and by 1933, it began development with an initial oil production rate of about 20,000 tons per day. The exploration well No. 45, drilled 1.5 km from the volcano’s crater in the mudfield, proved the feasibility of drilling in areas complicated by mud volcanism.

The field contains several productive horizons, which is penetrated by a central channel. At present, the Lokbatan oil field is in the final stage of development.



A — structure in VI Horizon Top; accumulation in VI–VIa horizons, B — field cross-section: scheme of flat sheet pools broken into blocks. 1 — oil; 2 — gas

Fig. 2. The schematic map of the Lokbatan oil field location (Zhemeriev, 1958, Martynova et al., 2022)

The Lokbatan anticline is composed of Pliocene-Quaternary deposits and is associated with a major longitudinal fault, which displaces strata of the same age by 300–350 meters. On the outside, the volcano is protected from erosion by a ridge of Absheron limestone and sandstones of the productive strata.

A particularly interesting fact about the Lokbatan mud volcano is the absence of a typical mud cone field, as well as the lack of small gryphons and salsas within its crater area, which are commonly observed at other mud volcanoes. In most volcanoes, during the inactive stage, water, liquid mud, and gas are usually released through these gryphons and

salsas. However, in the case of Lokbatan, the volcano's surface remains dry. A similar phenomenon is observed in only one other known case – the largest volcano of the Kerch Peninsula, Dzhau-Tepe – which also lacks a gryphon-salsa developmental stage (Shnyukov, 2006).

The main crater of the Lokbatan volcano formed after the eruption of 1887 and represents a subsidence caldera of oval shape with a diameter of 25 meters. The area covered by mud-volcanic material is about 424 hectares, and the average thickness of the erupted deposits reaches 60 meters. The elongated flow of mud-volcanic deposits,

observed in Fig. 1, extends 700 meters and has a western direction.

According to seismic studies, the Lokbatan mud volcano has a two-chamber structure (Kadirov, & Mukhtarov, 2004; Aliyev et al., 2013; Rashidov, Khasaeva, & Guseynov, 2016). The first, upper chamber is located at a depth of 1.5–2 km and lies within the deposits of the Quaternary system, while the second chamber is located in Neogene deposits at a depth of 4–6 km. The second chamber has periodic connections with productive oil-bearing horizons (Fig. 3) (Rashidov, Khasaeva, & Huseynov, 2016; Alizade, 2007).

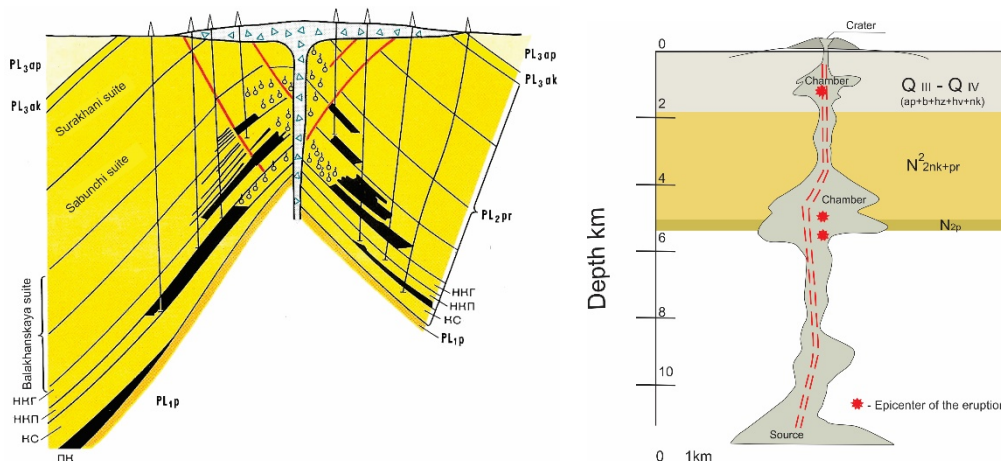


Fig. 3. Geological cross-section (a) (Aliyev et al., 2015) and conceptual model of the internal structure (b) of the Lokbatan mud volcano (Rashidov, Khasaeva, & Huseynov, 2016)

Field observations have shown that during an active eruption, the volcano ejects a large volume of a gas mixture (methane, carbon dioxide), steam, water, liquid mud, and breccia, forming a distinctive fountain reaching several hundred meters in height (Aliyev et al., 2013). The photo (Fig. 6) shows several moments of the volcano's eruption in 2012. Initially, there was an emission of steam and gas, followed by spontaneous ignition, and then the eruption of mud and breccia. Methane was the main gas component released during the eruption – accounting for 90–95 %. The carbon dioxide content reached 3–5 %. Nitrogen and hydrogen sulfide were also recorded in small amounts (Fig. 4). The gas sampled during the eruption on September 20, 2012, for isotopic analysis indicated a thermogenic origin of methane ($\delta^{13}CCH_4 \sim -48\%$) (Farber, Schmidt, & Feyzullayev, 2015).

The erupted liquid mud contains rock fragments of various sizes. Together with clay, they form what is known

as "mud breccia". Often, large rock fragments separate from the main mass during an eruption and scatter in different directions above the fountain, resembling volcanic "bombs". These fragments are composed of oil-bearing sandstones and combustible shales from the productive Eocene-Miocene age. The clay matrix of the erupted mud mainly consists of kaolinite and hydrosmeectite. The smectite content in the mud does not exceed 5–15 %. The Eocene-age combustible shales are enriched with organic matter significantly more (31.7 %) compared to Miocene shales (16.9 %). These shales generate gaseous and liquid hydrocarbons. The sandstone fragments from the eruptions are heavily impregnated with oil (Fig. 5) (Guliyev et al., 2017).

The oil is heavy, naphthene-aromatic, with a high concentration of resins (up to 20 %) and asphaltenes (up to 10 %). The content of oil fractions is up to 50 % (Guliyev et al., 2017).

Phase composition of gases released by Lokbatan volcano

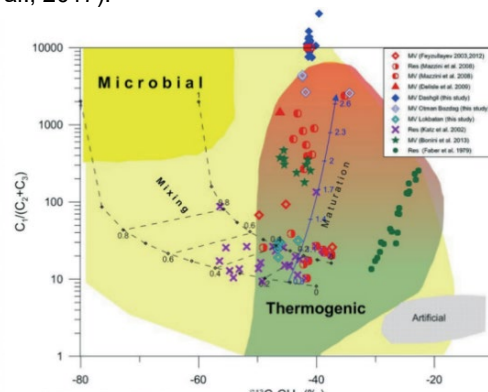
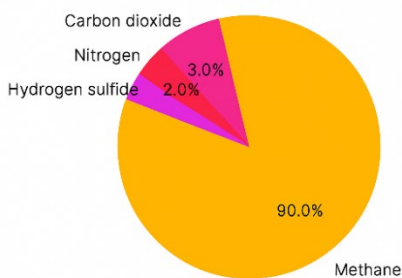


Fig. 4. Component composition of gases from the Lokbatan mud volcano (a); Gas data from hydrocarbon reservoirs collected from various fields and mud volcanoes in Azerbaijan (b) (Farber, Schmidt, & Feyzullayev, 2015)



Fig. 5 Oil-bearing sandstone and combustible shale in the mud breccia of the Lokbatan mud volcano (Aliyev et al., 2015)

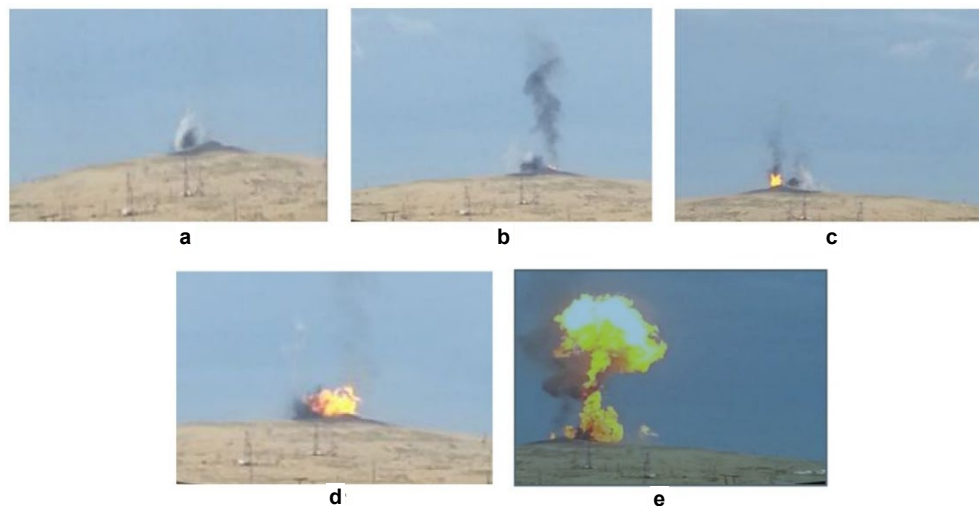


Fig. 6. Sequential moments of the Lokbatan mud volcano eruption in 2012 (Aliyev et al., 2013):

- a) beginning of the eruption phase, eruption of breccia and steam; b) increase in intensity of breccia and steam eruption; c) ignition of the intermediate focus; d, e) ignition of the entire gas eruption column

The Lokbatan deposit is a multi-layered structure, with productive horizons that are significantly isolated from one another, which is reflected in the composition of hydrocarbon from different depths.

For a long time, it was believed that the central eruptive channel of the mud volcano, by piercing all the productive horizons from bottom to top, connected them into a single unit, averaged the composition of hydrocarbons, and contributed to the rapid depletion of reserves through this channel. However, this hypothesis has not been confirmed for this volcano. Hydrocarbon emissions occur only during the active phase of eruptions, and between eruptions, the volcano does not release hydrocarbons.

This suggests that the productive horizons, divided into two wings, become isolated from the eruptive channel after the active phase by impermeable clayey rocks that prevent the hydrocarbons from migrating. For the same reason, no water is emitted from the volcano between cycles of active eruption, meaning it remains "dry". When the pressure in the productive horizons reaches an anomalous value, the clay plug is breached, and the entire water-gas-mud-oil mixture rises through the central channel.

Seismic events in the region likely contribute to the creation of a brief impulse that increases the pressure on the reservoir.

The first documented eruption of the Lokbatan mud volcano was in 1828 (Gamba, 1828). Periods of increased activity include eruptions occurring with small intervals of 2 to 5 years, from 1915 to 1941, during which 8 eruptions were recorded. Periods of decreased activity included the period from 1828 to 1900, with only 5 eruptions (Aliyev, Guliyev, &

Rahmanov, 2019). Currently, we are observing another period of increased mud volcanic activity. The most recent eruption was recorded in September 2024 (Fig. 7).

The water index of the Lokbatan volcano, like many others, had not been investigated before.

The idea occurred during the annual international summer school on "Mud Volcanism and Hydrocarbon Systems", which has been held since 2018 in Baku. We noticed the observable "dryness" of the mud flow and the absence of salsas emissions, which made the Lokbatan volcano stand out among others.

For satellite monitoring of the fluid (water) regime of the volcano, the Sentinel-2 satellite was selected in combination with the NDWI (Normalized Difference Water Index). This index was first proposed by McFeeters in 1996 to detect surface water in wetland environments and measure the area of open water surfaces (McFeeters, 1996). Thus, the NDWI is used to identify water bodies and assess soil moisture based on multispectral satellite imagery (Gao, 1996).

Recent studies have expanded the application of NDWI in mud volcano research, demonstrating its effectiveness for surface water and fluid regime monitoring. For example, investigated land cover characteristics of the Kesongo Mud Volcano Complex on Java Island, Indonesia, using harmonized Sentinel-2A MSI imagery to analyze surface features and provide visual interpretation of the fluid regime (Harbowo, & Sitingjak, 2025). Similarly, NDWI was successfully applied to predict the extent of the Sidoarjo mud flow, highlighting the method's potential for monitoring mud volcanic activity and associated hazards (Wicaksono, & Isa, 2022).

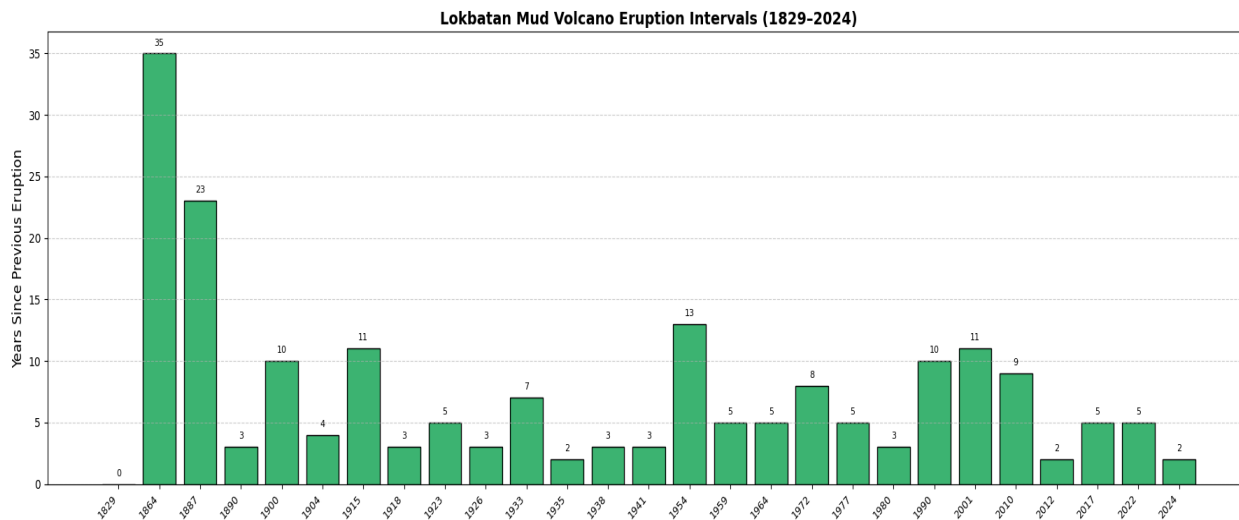


Fig. 7. Dynamics of Eruptions of Lokbatan Mud Volcano (Aliyev, Guliyev, & Rahmanov, 2019)

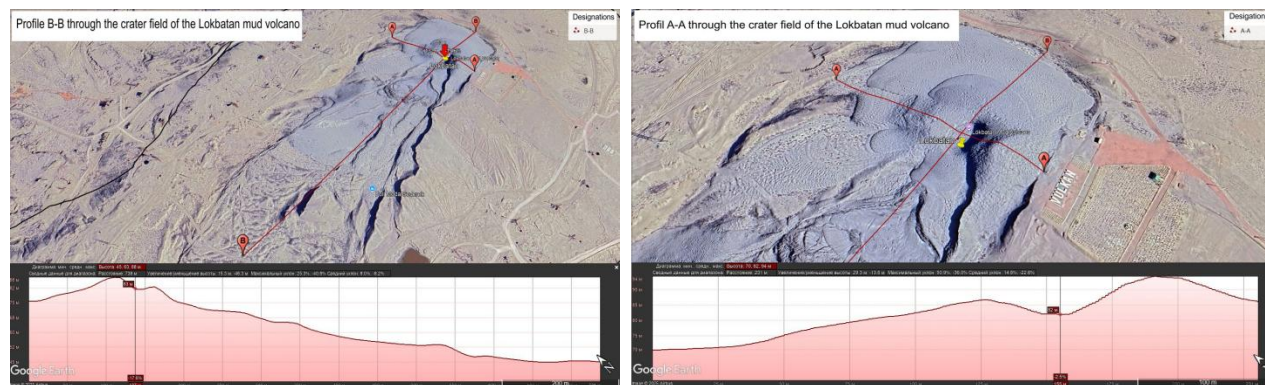


Fig. 8. Morphological Features of the Lokbatan Mud Volcano Based on Google Earth Data: a) – Across the Crater Field and b) – Along the "Tongues" of Breccia Outflows

In light of these developments, the current study not only utilizes Sentinel-2 data combined with NDWI but also aims to synthesize previous research experiences, emphasizing the novelty and applicability of this integrated methodology for assessing the fluid dynamics of mud volcanoes in the Absheron region. This approach offers a promising tool for enhanced remote monitoring, risk assessment, and early warning of mud volcanic and seismic hazards.

Despite the fact that initially for NDWI calculations it was supposed to use images obtained only from the Landsat Multispectral Scanner (MSS) satellite, it is worth noting that this method also worked well when using images from other satellites when there was a need for such an assessment (McFeeters, 1996; Chowdary et al., 2008; Environmental Protection Agency, 2005; Murray, 2012; Panigrahy, 2012; US Geological Survey..., 2013).

The NDWI is calculated using the following formula (1):

$$NDWI = \frac{(Band\ 2 - Band\ 4)}{(Band\ 2 + Band\ 4)}, \quad (1)$$

where Band 2 represents green light reflectance at the TOA (Top of Atmosphere) level, and Band 4 corresponds to near-infrared (NIR) reflectance. According to McFeeters (1996), NDWI values greater than zero are assumed to indicate the presence of water surfaces, while values less than or equal to zero generally correspond to non-water surfaces.

Thus, NDWI values range from -1 to 1, where higher index values are typically associated with water bodies or, in our case, areas with moist soil, whereas lower values indicate dry, non-water surfaces. It should be noted that data obtained from the Sentinel-2 satellite in open access reflect the spectral characteristics of the Earth's surface and require additional analytical processing, as well as integration with other data sources for comprehensive interpretation.

To analyze the dynamics of the fluid (water) regime of the Lokbatan mud volcano during the 2017–2023 period, which included two recorded eruptions, a satellite monitoring approach was applied. The use of satellite data enabled a detailed investigation of surface changes in the volcano area. The action algorithm included several key steps: 1) collection of satellite images and their calibration; 2) identification of fluid processes; 3) time series analysis; 4) mapping of changes; 5) interpretation of the obtained data and formulation of conclusions.

During processing, the NDWI formula was applied to the acquired multispectral satellite images. As a result, a KMZ file was generated, representing NDWI values for the researched area (Fig. 9). Then, NDWI values were extracted from image pixels along profile A-A (through the crater). These values were then plotted on a time-series graph showing the distribution of NDWI over time (Fig. 10).

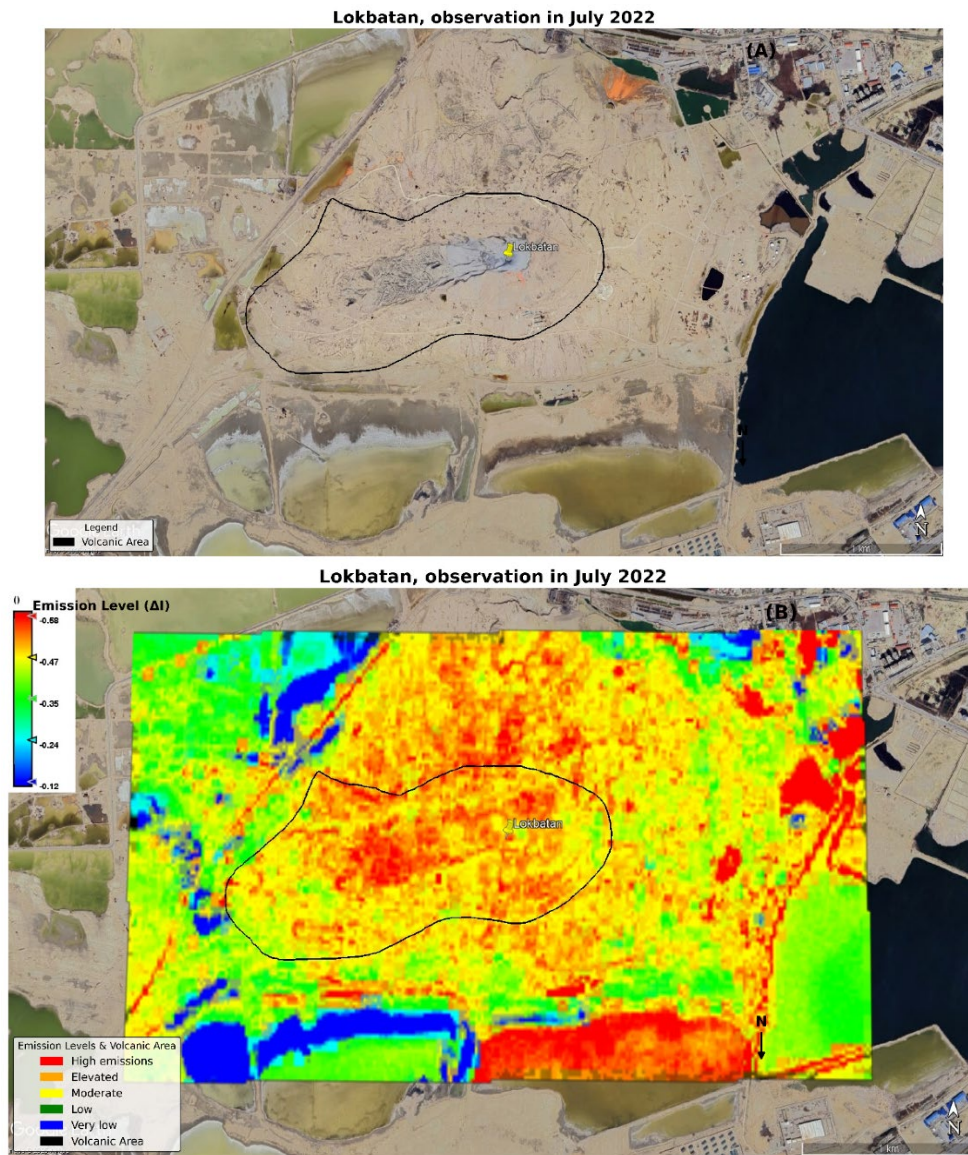


Fig. 9. Map of the Moisture Index Distribution at the Lokbatan Mud Volcano for the 2022:
 a) Satellite image of the Lokbatan mud volcano, b) map of moisture Index (NDWI) distribution for the Lokbatan area

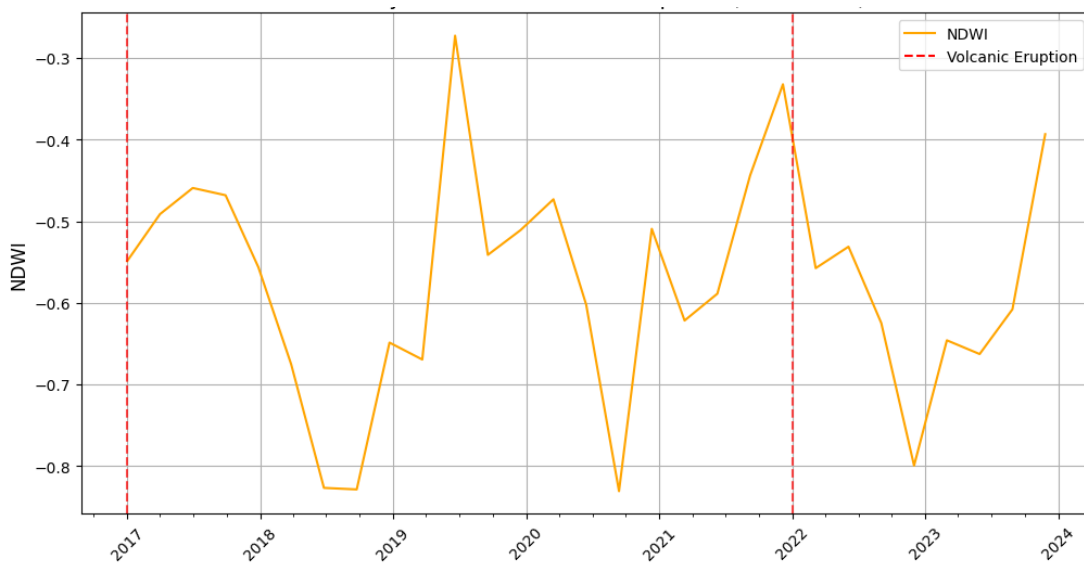


Fig. 10. Plot of NDWI and Eruption variation on the Lokbatan mud volcano from 2017 to 2023

Results

During the aforementioned period, a comprehensive set of monitoring activities was carried out for the Lokbatan mud volcano. According to satellite data, the analysis of the moisture index of the mud volcanic cover, influenced by various factors including geological activity and climate changes, revealed the following trends and factors:

- **Climate factor** – the moisture of the mud volcanic cover positively correlates with seasonal and climatic changes.

- **Earthquakes and geodynamic activity** – recorded earthquakes, especially in 2020, 2021 and 2022, probably have an influence on moisture and may be predictors of changes in the geodynamic conditions, as well as sometimes preceding volcanic activity.

- **Anomalies in the moisture index** – sudden changes in moisture, anomalous peaks, and stable values during certain periods can serve as indicators of potential risks of volcanic activity.

- **Forecasting volcanic activity** – before the eruption in August 2022, anomalies in the water regime of the mud volcano were observed in February. This could serve as an indicator for predicting paroxysmal events.

In **2017**, the NDWI values in the Lokbatan mud volcano and its surroundings had significant fluctuations, from minimum to maximum values. In 2017, the humidity index values in the volcano and its surroundings had significant fluctuations, from minimum to maximum values, which was the result of several factors at once – seasonal fluctuations, which were most pronounced in the summer, and volcanic activity, which manifested itself in the form of the 25th eruption, which led to a sharp increase in the moisture index. By autumn, NDWI values reached a minimum value. However, by the end of the year, a gradual increase in NDWI values was observed, especially in the central (crater) part of the Lokbatan mud volcano.

In **2018**, the humidity index values also showed considerable fluctuations; however, the overall trend indicated a gradual increase, most likely due to climatic factors (seasonal variations) as well as hydrogeological processes.

At the beginning of **2019**, NDWI values remained relatively stable, but in May, a sharp drop to -1 was recorded. By summer, the index had risen slightly to -0.78, only to decline again in winter, reaching a minimum value of -0.96.

At the beginning of **2020**, an increase in NDWI values was observed, followed by a decline during the spring period. The summer season was characterized by relatively stable NDWI values. However, by October, a sharp increase to -1 was recorded, followed by a return to minimum values in December. It is also worth noting that on February 15, an earthquake with a magnitude of 4.6 was recorded near the mud volcano at a depth of approximately 30 km, which may have influenced the overall NDWI trend for 2020.

Throughout **2021**, fluctuations in NDWI values were recorded at the Lokbatan mud volcano. In early February, the NDWI value was -0.45, but from March to May, it dropped to -0.65. Additionally, earthquakes with magnitudes of 4.1 and 5.0 were recorded in August and November, respectively, which undoubtedly affected the geodynamic activity in the region.

It is noteworthy that in December, NDWI values in the southwestern part of the Lokbatan mud volcano reached -0.94, in the central (crater) part -1, and in the mudflow "tongue" area -0.55.

In **2022**, on August 11, the Republican Seismological Service Center recorded an eruption of the Lokbatan mud volcano that lasted 5 minutes and 12 seconds ($E=0.6 \times 10^7$), along with two earthquakes: one in February with a magnitude of 4.2 at a depth of 56 km, and another in August with the same magnitude at a depth of 62 km. These events, to some extent, were reflected in the NDWI values. The NDWI values for the first half of 2022 remained relatively stable at -0.76. However, a sharp spike in NDWI values was observed in the crater area in February, reaching -1.

The year **2023** was characterized by relatively stable NDWI values. However, an increase in NDWI values up to -1 was observed in the crater area at the beginning of the year.

The anomalies in NDWI values observed in the middle and end of the year in the crater area may be due to some volcanic activity or seasonal environmental changes. According to the data collected for 2023, the average NDWI value for the crater area was -0.81, with a maximum value of -1 and a minimum of -0.57.

Based on the accumulated satellite data on NDWI for the Lokbatan mud volcano, its variations, and observed trends during the 2017–2023 period, a statistical forecast can be made regarding the expected behavior of NDWI values for the coming years. Using linear variation, we attempted to make such a forecast for the period from 2024 to 2030 (Fig. 11).

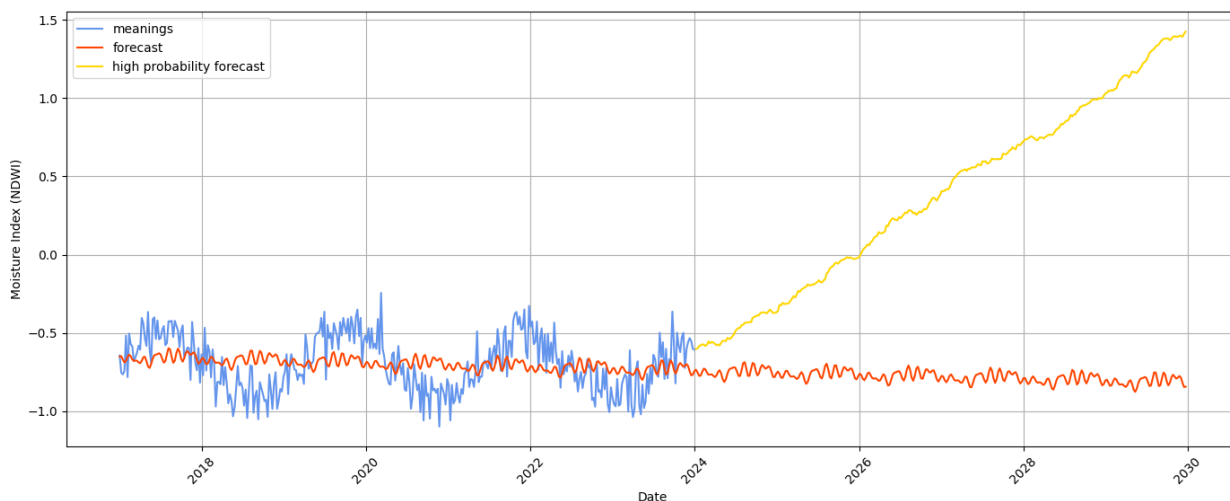


Fig. 11. Assessment of probable variations in the moisture index until 2030

The accuracy of the estimated data can be judged by the calculations for 2024, where the actual values almost coincide with the predicted ones. At the beginning of 2024, the high-probability trend shows fluctuations, then begins to rise in June, reaching a peak by the end of the year. An anomaly stands out in late June – early July, where a sharp increase in value occurs. The average value rises sharply from -0.39 to 0.07. In 2025, the high-probability trend fluctuates between 0.26 and 0.77 from January to June, with a sharp increase in June–July. An anomaly in October–November, expressed by growth, also stands out.

The graph titled "Assessment of probable changes in the moisture index until 2030" presents two main forecast components:

● The blue line represents the historical values of the moisture index, collected over the period from 2017 to 2024.

● The orange line shows the forecast, calculated using time series models such as Prophet, which take into account both trends and seasonal components. This forecast is based on historical data up to 2024 and extrapolates it into the future until 2030. The methodology assumes the continuation of current trends and seasonal patterns. The "forecast" has a broader uncertainty range, as it includes all possible scenarios – both favorable and unfavorable – without filtering by probability. This makes it suitable for assessing the overall range of moisture index fluctuations, assuming external factors remain unchanged.

● The yellow line represents the high probability forecast – the most likely scenario of future development, derived from a confidence interval (typically 95 %). It can be constructed using Bayesian or ensemble modeling methods, where the result reflects an average trajectory (e.g., the median) across multiple simulations. Unlike the full forecast, this component focuses on the statistically dominant scenario, excluding extreme variations. Thus, the "high probability forecast" reflects an optimistic yet realistic vector of potential changes in the moisture index, given the current trends.

Discussion and conclusions

Monitoring the Lokbatan mud volcanic activity using satellite data has shown positive results and can be effectively applied in future comprehensive studies of mud volcanism dynamics.

The fluid regime of the Lokbatan mud volcano during the study period was influenced by both geodynamic and climatic factors, which was reflected in variations of the moisture index.

The behavior of the moisture index under climatic influence differs from that caused by geodynamic factors by the "smoothness" of value changes and its clear seasonal dependence. In contrast, geodynamic factors tend to be associated with more abrupt "spikes" in the humidity index values, standing out against the general background – for example:

- Earthquakes can affect internal hydrodynamic processes within the mud volcano, leading to fluctuations in the moisture index (as observed with earthquakes in 2020, 2021, and 2022 within a 100 km radius of the Lokbatan mud volcano).

- Sudden changes in the moisture index on the mud volcano can be considered an additional mechanism for assessing potential upcoming volcanic activity (as demonstrated in the 2022 data analysis).

In conclusion, the interconnection between geological processes, climatic factors, and seismic activity represents a complex and demanding process that requires extensive data analysis and systematic monitoring. This approach is

essential for effectively responding to both actual and potential risks associated with mud volcanoes.

Therefore, analyzing changes in the water regime of mud volcanoes based on satellite data – using the Lokbatan mud volcano as an example – can serve as an additional tool for anticipating future paroxysms. Satellite moisture analysis provides crucial insights into the dynamics of volcanic processes, contributing to the development of monitoring and forecasting systems for volcanic activity. However, further and more detailed studies are necessary.

Authors' contributions: Arif Huseynov – conceptualization, methodology, software, formal analysis, data validation, writing (original draft). Viktor Nesterovskiy – writing (review and editing); Ayten Huseynova – data validation, writing (original draft).

References

- Aliyev, A., Guliyev, I., Dadashov, F., & Rahmanov, R. (2015). *Atlas of the world mud volcanoes*. Nafta&Press, Sandro Teti Editori.
- Aliyev, A., Guliyev, I., & Rahmanov, R. (2019). *Catalogue of recorded mud volcano eruptions of Azerbaijan (2008–2018)*. Elm.
- Aliyev, G. G., Guliyev, I. S., Yetirmishli, G. et al. (2013). The eruption of the Lokbatan mud volcano on September 20, 2012: New evidence for the replenishment of hydrocarbon resources. *ANAS Transactions. Earth Sciences*, 2, 18–25 [in Russian]. [Алиев, Г. Г., Гулиев, И. С., Йетирмишли, Г. и др. (2013). Извержение грязевого вулкана Локбатан 20 сентября 2012 г.: новые свидетельства восполняемости ресурсов углеводородов. *Известия Национальной академии наук Азербайджана. Науки о Земле*, 2, 18–25].
- Alizade, A. A. (Ed.). (2007). *Geology of Azerbaijan: (in 8 volumes). Stratigraphy* (Vol. 1). Nafta-Press [in Russian]. [Ализаде, А. А. (Гл. ред.). (2007). *Геология Азербайджана: (в 8 томах). Стратиграфия* (Т. 1). Nafta-Press. с. 580].
- Chowdary, V. M., Chandran, R. V., Neeti, N., Bothale, R. V., Srivastava, Y. K., Ingle, P., Ramakrishnan, D., Dutta, D., Jeyaram, A., Sharma, J. R. et al. (2008). Assessment of surface and sub-surface waterlogged areas in irrigation command areas of Bihar state using remote sensing and GIS. *Agricultural Water Management*, 95(7), 754–766.
- Environmental Protection Agency (EPA). (2005). *Wetland Mapping and Classification Methodology – Overall Framework – A Method to Provide Baseline Mapping and Classification for Wetlands in Queensland* (Version 1.2). Queensland Government.
- Farber, E., Schmidt, M., & Feyzullayev, A. (2015). Geochemical Hydrocarbon Exploration – Insights from Stable Isotope Models. *Oil Gas European Magazine*, 41(2), 93–98.
- Gamba, J. F. (1828). Earthquake and eruption of a new fire-breathing mountain near Baku. *Sev. archive*, 34(7), 161–162 [in Russian]. [Гамба, Ж. Ф. (1828). Землетрясение и извержение новой огнедышащей горы близ Баку. *Сев. архив*, 34(7), 161–162].
- Gao, B.-C. (1996). NDWI – A normalized difference water index for remote sensing of vegetation liquid water from space. *Remote Sensing of Environment*, 58, 257–266.
- Guliyev, I., Kerimov, V., Osipov, A. et al. (2017). Generation and Accumulation of Hydrocarbons at Great Depths Under the Earth's Crust. *SOCAR Proceedings*, 1, 004–016 [in Russian]. [Гулиев, И. С., Керимов, В. Ю., Осипов, А. В. и др. (2017). Генерация и аккумуляция углеводородов в условиях больших глубин земной коры. *SOCAR Proceedings*, 1, 004–016]. <https://doi.org/10.5510/OGP20170100302>
- Harbowo, D. G., & Sitingjak, E. S. (2025, February). *Investigating the Land Cover Characteristics of the Kesongo Mud Volcano Complex, Java Island, Indonesia: Surface Analysis and Visual Interpretation through Harmonized Sentinel-2A MSI Imagery*. Paper presented at the IOP Conference Series: Earth and Environmental Science, Indonesia.
- Kadirov, F. A., & Mukhtarov, A. Sh. (2004). Geophysical Fields, Deep Structure, and Dynamics of the Lokbatan Mud Volcano. *Izvestiya, Physics of the Solid Earth*, 40(4), 67–73 [in Russian]. [Кадиров, Ф. А., & Мухтаров, А. Ш. (2004). Геофизические поля, глубинное строение и динамика грязевого вулкана Локбатан. *Физика Земли*, 40(4), 67–73].
- Martynova, G. S., Maksakova, O. P., Nanadzhanova, N. I. et al. (2022). Lokbatan oil field. *Oil and Gas Geology*, 2, 45–52 [in Russian]. [Мартынова, Г. С., Максакова, О. П., Нанаджанова, Н. И. и др. (2022). Месторождение нефти Локбатан. *Геология нефти и газа*, 2, 45–52. <https://doi.org/10.31087/0016-7894-2022-2-45-52>].
- McFeeters, S. K. (1996). The use of the Normalized Difference Water Index (NDWI) in the delineation of open water features. *International Journal of Remote Sensing*, 17(7), 1425–1432.
- Murray, N. J., Phinn, S. R., Clemens, R. S. et al. (2012). Continental scale mapping of tidal flats across East Asia using the Landsat archive. *Remote Sensing*, 4(11), 3417–3426.
- Panigrahy, S., Murthy, T. V. R., Patel, J. G. et al. (2012). Wetlands of India: Inventory and assessment at 1:50,000 scale using geospatial techniques. *Current Science*, 102(6), 852–856.

Rashidov, T., Khasayeva, A., & Huseynov, A. (2016). On issue of the mud volcano Lokbatan inner structure. *Geophysics News in Azerbaijan*, 1–2, 41–44 [in Russian]. [Рашидов, Т. М., Хасаева, А. Б., & Гусейнов, А. Р. (2016). К вопросу о внутреннем строении грязевого вулкана Локбатан. *Azerbaijanda Geofizika Yeniliklari*, 1–2, 41–44].

Shnyukov, E. F. (2006). *Mud volcanoes of the Kerch-Taman region*. GlavMedia [in Russian]. [Шнюков, Е. Ф. (2006). *Грязевые вулканы Керченско-Таманского рееиона*. ГлавМедиа].

Wicaksono, W., & Isa, S. M. (2022). Predicting the Extent of Sidoarjo Mud Flow Using Remote Sensing. *Journal of ICT Research & Applications*, 16(1).

Yakubov, A. A., Aliyev, A. A., & Rakhmanov, R. R. (1976b). *Mud volcanoes of Azerbaijan (annotated bibliographic reference)*. Elm [in Russian]. [Якубов, А. А., Алиев, А. А., & Рахманов, Р. Р. (1976b). *Грязевые вулканы Азербайджана (аннотированный библиографический справочник)*. Элм].

Yakubov, A. A., Kastruyilin, N. S., & Javadov, A. A. (1976a). *Mud volcanism and oil and gas potential of Lokbatan*. Elm [in Russian]. [Якубов, А. А., Кастрюлин, Н. С., & Джавадов, А. А. (1976a). *Грязевой вулканизм и нефтегазоносность Локбатана*. Элм].

Zhemerev, V. S. (1958). Changes in the nature of waters during the exploitation of oil horizons in Lokbatan. *Geology of Oil*, 11, 45–50 [in Russian]. [Жемерев, В. С. (1958). Изменение характера вод в процессе эксплуатации нефтяных горизонтов в Локбатане. *Геология нефти*, 11, 45–50].

US Geological Survey (USGS) and US Department of the Interior. (2013, May 3). *Normalized Difference Water Index (NDWI)*. Retrieved July 8, 2025, from http://deltas.usgs.gov/fm/data/data_ndwi.aspx

The history of the famous oil well "No. 45" and the mud volcano in Lokbatan – UNKNOWN FACTS – PHOTO. (2022, November 29). *Day.Az*. [in Russian]. [История знаменитой нефтяной скважины "№45" и грязевого вулкана в

Локбатане – НЕИЗВЕСТНЫЕ ФАКТЫ – ФОТО (2022). *Day.Az*. <https://news.day.az/society/1469420.html>

US Geological Survey. (n.d.). *Earthquakes map* (2020). Retrieved July 8, 2025, from <https://earthquake.usgs.gov/earthquakes/map/?extent=38.52668,46.79077&extent=41.56614,53.82202&range=search&search=%7B%22name%22:%22Search%20Results%22,%22params%22:%22starttime%22:%222020-01-01%2000:00:00%22,%22endtime%22:%222020-12-31%2023:59:59%22,%22latitude%22:40.3,%22longitude%22:49.7,%22maxradiuskm%22:100,%22minmagnitude%22:2.5,%22eventtype%22:%22earthquake%22,%22orderby%22:%22time%22%7D%7D>

US Geological Survey. (n.d.). *Earthquakes map* (2021). Retrieved July 8, 2025, from <https://earthquake.usgs.gov/earthquakes/map/?extent=38.66407,407.01599&extent=41.69753,414.04724&range=search&search=%7B%22name%22:%22Search%20Results%22,%22params%22:%22starttime%22:%222021-01-01%2000:00:00%22,%22endtime%22:%222021-12-31%2023:59:59%22,%22latitude%22:40.3,%22longitude%22:49.7,%22maxradiuskm%22:100,%22minmagnitude%22:2.5,%22eventtype%22:%22earthquake%22,%22orderby%22:%22time%22%7D%7D>

US Geological Survey. (n.d.). *Earthquakes map* (2023). Retrieved July 8, 2025, from <https://earthquake.usgs.gov/earthquakes/map/?extent=36.61553,41.4624&extent=48.28319,69.5874&range=search&search=%7B%22name%22:%22Search%20Results%22,%22params%22:%22starttime%22:%222023-02-21%2000:00:00%22,%22endtime%22:%222023-12-28%2023:59:59%22,%22latitude%22:40.3,%22longitude%22:49.7,%22maxradiuskm%22:100,%22minmagnitude%22:2.5,%22eventtype%22:%22earthquake%22,%22orderby%22:%22time%22%7D%7D>

Отримано редакцією журналу / Received: 23.01.25
Прорецензовано / Revised: 20.02.25
Схвалено до друку / Accepted: 30.06.25

Аріф ГУСЕЙНОВ, магістр наук про Землю

ORCID ID: 0000-0002-9941-3221

e-mail: huseynovarif85@gmail.com

Інститут нафти і газу, Міністерство науки і освіти Азербайджану, Баку, Азербайджан

Віктор НЕСТЕРОВСЬКИЙ, д-р геол. наук, проф.

ORCID ID: 0000-0002-7065-8962

e-mail: v.nesterovski@ukr.net

Київський національний університет імені Тараса Шевченка, Київ, Україна

Айтен ГУСЕЙНОВА, канд. геол. наук

ORCID ID: 0000-0002-1932-4289

e-mail: aytenhuseynova@anas.az

Президія Національної академії наук Азербайджану, Баку, Азербайджан

ПЕРШИЙ ДОСВІД ВИКОРИСТАННЯ СУПУТНИКОВИХ ДАНИХ ДЛЯ МОНІТОРИНГУ ВОДНО-ФЛЮЇДНОГО РЕЖИМУ ВУЛКАНА ЛОКБАТАН ПРИ ОЦІНЦІ РИЗИКІВ СЕЙСМІЧНИХ ПОДІЙ У РЕГІОНІ

В с т у п . Грязеві вулкани є активними природними структурами, що впливають на навколишнє середовище шляхом безперервних викидів газорідних флюїдів, грязьової брекчії та грязьових потоків. Попри широкі дослідження та значний масив даних про грязьовий вулканизм, розуміння динаміки флюїдів та гідрогеологічних процесів, пов'язаних із цими системами, залишається предметом постійних дискусій. Нині налічується понад 2500 грязьових вулканів, розташованих у 42 країнах світу, що підкреслює їх глобальне поширення.

Територія Азербайджану – унікальний регіон для дослідження сучасного грязьового вулканизму. На його порівняно невеликій території розташовано понад 350 грязьових вулканів. Грязьовий вулкан Локбатан серед них є найактивнішим. На ньому зареєстровано 28 активних подій з виверженням великої кількості матеріалу, з ним пов'язане нафтове родовище і сейсмічні події. У цьому контексті комплексний підхід до вивчення активності грязьових вулканів, включаючи супутниковий моніторинг, є надзвичайно актуальним.

М е т о д и . У роботі використано методи дистанційного зондування для аналізу водно-флюїдного режиму грязьового вулкана Локбатан, фіксації активних фаз і пошуку кореляційних зв'язків. Зокрема, супутникові знімки застосовано для розрахунку індексу вологості у межах грязевулканічного поля, що періодично змінюється. Вперше цей індекс виміряно дистанційно, що дало змогу оцінити динаміку поверхневої вологості як показник міграції флюїдів та підповерхневої активності.

Р е з у л ь т а т и . Отриманий за допомогою супутника індекс вологості показав чіткі кореляції з активністю грязьового вулкана. Спостереження вказують на те, що варіації індексу вологості відповідають змінам у флюїдному режимі грязевулканічної структури, відображаючи можливу підземну міграцію флюїдів або зміни тиску перед фазою виверження.

В и с н о в к и . Дослідження демонструє потенціал супутникового моніторингу в оцінці водно-флюїдного режиму інших активних грязьових вулканів. Цей підхід може забезпечити ефективну, недорогу альтернативу польовим спостереженням і лабораторним дослідженням і надає можливість підтримувати системи раннього попередження про сейсмічні події чи виверження. У подальшому отриманий досвід можна реалізувати при розробці превентивних стратегій управління геологічними процесами в сейсмічно активних регіонах.

К л ю ч о в і с л о в а : грязьовий вулкан Локбатан, супутникові знімки, флюїди, NDWI, моніторинг.

Автори заявляють про відсутність конфлікту інтересів. Спонсори не брали участі в розробленні дослідження; у зборі, аналізі чи інтерпретації даних; у написанні рукопису; в рішенні про публікацію результатів.

The authors declare no conflicts of interest. The funders had no role in the design of the study; in the collection, analyses or interpretation of data; in the writing of the manuscript; or in the decision to publish the results.

UDC 004.891:528.4

DOI: <http://doi.org/10.17721/1728-2713.110.13>

Vasyl HUDAK¹, PhD Student
 ORCID ID: 0009-0002-7333-0409
 e-mail: gudak_vasyl@knu.ua

Serhii MARHES², PhD Student
 ORCID ID: 0009-0004-2942-9406
 e-mail: sergemarhes@gmail.com

Vitalii ZATSERKOVNYI¹, DSc (Techn.), Prof.
 ORCID ID: 0009-0003-5187-6125
 e-mail: vitalii.zatserkovnyi@knu.ua

Mauro DE DONATIS³, PhD (Geol.), Assoc. Prof.
 ORCID ID: 0000-0002-9721-1095
 e-mail: mauro.dedonatis@uniurb.it

¹Taras Shevchenko National University of Kyiv, Kyiv, Ukraine

²State Institution "Scientific Centre for Aerospace Research of the Earth of the Institute of Geological Sciences of the National Academy of Sciences of Ukraine", Kyiv, Ukraine

³University of Urbino Carlo Bo, Urbino, Italy

METHODOLOGY FOR THE AUTOMATED DETECTION OF ANOMALOUS GEOSPATIAL ZONES IN SATELLITE IMAGERY USING STATISTICAL ANALYSIS AND A CUSTOM QGIS PLUGIN

(Представлено членом редакційної колегії д-ром геогр. наук, проф. Д.О. Ляшенко)

Background. This article presents a methodology for the automated detection of anomalous geospatial zones, implemented as a plugin for the QGIS geographic information system. The developed tool enhances the efficiency of spatial analysis and enables the rapid identification of areas with potential changes for monitoring natural and anthropogenic processes.

Methods. The proposed approach is based on thresholding and statistical analysis of satellite imagery within the QGIS environment. The plugin provides interactive adjustment of image processing parameters and automatically detects geodynamic anomalies, which are then vectorized and delivered to the user for further analysis. The algorithm utilizes Python libraries (NumPy, SciPy, GDAL, PyQt, QGIS API) to handle various types of satellite data and applies standard deviation-based criteria to identify anomalous areas.

Results. The testing of the plugin developed by the authors confirmed its effectiveness in processing satellite imagery types such as InSAR, thermal infrared (TIR), and NDWI-based images. The plugin successfully identified areas of vertical displacement of the Earth's surface, detected thermal anomalies, and delineated regions with moisture deficits. This approach substantially improves the accuracy of geospatial analysis.

Conclusions. The developed plugin is an effective tool for the automated monitoring of changes in the Earth's surface and the assessment of hydrogeological conditions. Its integration within the QGIS environment enables the efficient adjustment of analysis parameters and the generation of results in vector data format. Plugin testing confirmed its practical value and revealed potential directions for further improvement, particularly regarding the separate processing of positive and negative displacement values to enhance the accuracy of anomaly interpretation.

Keywords: automated detection, geospatial zones, QGIS plugin, satellite imagery, geodynamic anomalies, spatial analysis.

Background

In the modern, rapidly changing world, various types of emergencies increasingly arise, including natural disasters, military conflicts, and man-made accidents. In such situations, rapid response is critically important, as it involves assessing the situation and making optimal or efficient decisions to mitigate negative consequences. However, the process of territorial assessment is often time-consuming and complex due to the large volume of data that must be processed, as well as the lack of effective tools for timely data collection and analysis.

Contemporary methods for analyzing satellite imagery play a key role in monitoring environmental changes, assessing anthropogenic impacts, and detecting geodynamic processes. Nonetheless, traditional approaches such as visual interpretation and manual digitization have significant limitations when dealing with large-scale areas or vast datasets. Their effectiveness is often compromised by the subjectivity of interpretation, dependence on the operator's qualifications, and the difficulty of reproducing results, which complicates long-term analysis and automated change mapping. Therefore, new tools capable of automating these processes and enhancing the accuracy of outcomes are needed to

overcome these challenges and ensure timely analysis (Tempa, & Aryal, 2022).

Under these circumstances, the availability of a comprehensive tool capable of conducting rapid and accurate analysis of satellite images to detect destruction and assess the overall condition of affected areas becomes essential (MASAI Project, n.d.). Such tools represent a vital component for improving emergency response efficiency. The automation of satellite image analysis through the use of Geographic Information Systems (GIS) helps to minimize the shortcomings of traditional methods by standardizing the detection of anomalous zones that emerge as a result of image processing (Janz et al., 2021). In particular, geostatistical algorithms facilitate more accurate anomaly recognition, reduce the impact of data noise, and enhance overall analysis efficiency. The integration of such solutions into the QGIS environment opens new opportunities for automated monitoring of surface changes, especially in the context of hydrogeological condition assessments and the analysis of anthropogenic impacts (Ivanik et al., 2022).

This study presents a custom-developed plugin for the QGIS software that enables the identification of anomalous zones derived from satellite image processing – namely,

© Hudak Vasyl, Marhes Serhii, Zatserkovnyi Vitalii, De Donatis Mauro, 2025

areas that deviate from background values and indicate changes or anomalies within the studied region. A key feature of the plugin developed by the authors is its applicability to various types of satellite data. Specifically, the study demonstrates the use of the plugin with InSAR images, thermal infrared (TIR) imagery, and optical indices derived from multispectral images (e.g., NDWI in the green and near-infrared (NIR) bands). The plugin is lightweight and user-friendly, requiring no additional pre-processing or complex computations. The user simply uploads an image, defines parameters for extracting polygons with anomalous values, and the plugin automatically performs the analysis and generates results. The plugin is freely available under an open-access license at https://github.com/rnrhs/autocountour_qgis_plugin (Marhes, 2025), ensuring its broad accessibility to researchers and professionals working in the fields of remote sensing and geospatial technologies. Its open-source nature also allows for easy modification, extension of functionality, and integration into diverse analytical workflows, which is a crucial aspect for supporting both scientific research and applied engineering practices.

The primary objective of the developed plugin is the automated detection of anomalous zones that exceed

predefined threshold values, separating them from the main data array that does not meet the anomaly criteria. The threshold serves as a criterion for identifying deviations from the average or statistically expected values, enabling the extraction of geospatial objects with abnormal displacements or other parameters that warrant further analysis.

Methods

The algorithm governing user interaction with the plugin interface comprises a series of sequential steps designed to enable efficient processing of satellite imagery and the detection of zones with potential geodynamic anomalies (Fig. 1).

The image processing workflow within the developed plugin begins with its launch in the QGIS environment. Prior to this, the plugin must be installed following the official QGIS guidelines (QGIS Project, 2024). Subsequently, the user selects the raster image to be processed and adjusts the sensitivity parameters to configure anomaly detection settings. As the user modifies the sensitivity threshold, corresponding changes are dynamically visualized on the map, allowing threshold values to be fine-tuned through iterative selection to enhance the accuracy of anomaly detection. The final output is generated in the form of vector data, which is well-suited for further spatial analysis.



Fig. 1. Schematic representation of the sequence of user-side operations

The proposed QGIS plugin algorithm, grounded in statistical analysis and geoinformation approaches, facilitates the effective identification of anomalies in raster data by employing threshold-based and statistical techniques for the automated detection of anomalous regions in satellite imagery, followed by automatic vectorization of the results. The core principle of the algorithm is the assumption that anomalous values can be identified as deviations from the average statistical level, defined within a specified threshold coefficient.

Threshold analysis is based on determining a value beyond which the data are considered anomalous (Folini, Lenzi, & Biraghi, 2022). The threshold can be set manually or computed adaptively depending on the data distribution. Although this method is relatively straightforward to implement, it requires appropriate threshold selection to avoid false positives. The main stages of the threshold analysis include:

- noise removal and interpolation of missing values;
- determination of the threshold value – which can be specified by the user or automatically calculated (e.g., as a percentage of the maximum deviation or based on a histogram of data distribution);
- application of the threshold criterion – comparing each pixel to the threshold and highlighting zones exceeding this level, followed by contour smoothing;
- filtering of spurious regions.

Statistical analysis is employed to identify areas that significantly deviate from the average level of values. One common approach involves the use of standard deviation to detect anomalies:

$$x | x > \mu + k \sigma, \tag{1}$$

where μ denotes the mean value, σ the standard deviation, and k a coefficient defining the anomaly level.

This method accounts for statistical properties of the data distribution, thereby improving detection accuracy (Folini, Lenzi, & Biraghi, 2022).

Numerous statistical methods for anomaly detection are based on conventional statistical thresholds, classifying anomalies into weak (approximately 5 %) and strong (approximately 0.3 %) categories. These classifications rely on standard deviation metrics and the assumption of normal distribution (Cleveland, 1993; Zhukov, 2008; Meng et al., 2017), and form the basis for data classification. These principles underpin the proposed plugin algorithm for detecting anomalous zones in satellite imagery.

The algorithm is implemented in the QGIS plugin using several Python libraries:

- NumPy – for efficient statistical computations and array processing;
- SciPy – for mathematical analysis and spatial filtering techniques;
- GDAL – for handling geospatial data and raster image processing.

In addition to these statistical analysis libraries, the developed plugin also utilizes a number of other Python packages to ensure full functionality and seamless integration with QGIS. Notably, components from the PyQt library are imported to construct the graphical user interface for parameter configuration (QSettings), translations (QTranslator), core functionality (QCoreApplication), icon management (QIcon), and dialog windows (QAction).

For spatial data handling, the plugin uses QGIS libraries such as QgsProject, QgsRasterLayer, and QgsVectorLayer for managing projects and layers, QgsRasterBandStats for computing statistics, and QgsMessageLog for message logging. Additionally, the GDAL, OGR, and OSR libraries support the manipulation of raster and vector data, while NumPy provides the

computational backend. The plugin also integrates resources from an external file (`resources.py`) and implements a dialog window to facilitate user interaction (Fig. 2).

All raster and vector data processed within the system adhere to a unified coordinate reference system, which is essential for accurate integration and geospatial analysis. To ensure consistency, the plugin retrieves the coordinate system and projection information of the selected raster

layer. Initially, the active raster layer is identified via the map layer control element (`mMapLayerComboBox`). The data source path of the selected layer is then obtained, and the corresponding raster file is opened using the GDAL library. The `GetProjection()` method is employed to extract the layer's projection description in Well-Known Text (WKT) format, which enables precise identification of the spatial parameters and coordinate system of the data.

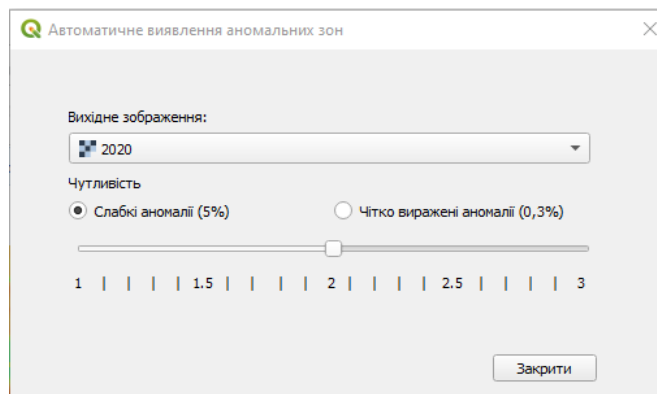


Fig. 2. User interaction dialog in the developed plugin

A detailed breakdown of the AutoContour plugin's functionality is provided to elucidate its underlying principles by separating it into distinct logical modules.

Plugin Initialization

The initialization process of the AutoContour plugin involves the import of essential libraries, including PyQt, the QGIS API, GDAL, OGR, and NumPy. At this stage, a reference to the QGIS interface is stored, enabling access to data and the ability to manage map layers. The plugin directory is also defined, and localization is configured based on the user's system settings. Variables are declared to store the paths of temporary raster and vector files that are generated and processed throughout the algorithm's execution. This design enhances the plugin's modularity and performance within the QGIS environment, while also preventing unnecessary file accumulation.

Graphical Interface and QGIS Integration

The integration of the plugin with the QGIS graphical interface is achieved through its registration in the software menu and the addition of the corresponding tools to the toolbar. This process is implemented using the `initGui()` method, which creates control elements such as buttons and menus, providing the user with access to the plugin's functionalities. The main element is the action (`QAction`), which is added to the toolbar and the 'Raster' menu, enabling the execution of the automatic contouring algorithm from the graphical interface. The plugin also supports the dynamic loading of localized resources, ensuring the correct display of interface elements according to the user's language settings.

For proper management of the plugin's operation, a mechanism for unloading is provided through the `unload()` method, which is responsible for clearing the interface and removing the corresponding menu items and buttons from the toolbar. User interaction with the algorithm is facilitated through the `AutocountourDialog` window, which allows the user to set processing parameters, such as the segmentation threshold. The window supports interactive adjustment of parameters, enabling real-time control over the analysis results. Thus, the developed architecture ensures flexible integration of the plugin into the QGIS environment and facilitates its use for spatial data analysis.

Raster Data Processing

The algorithm for processing raster data is based on their mathematical representation as a discrete two-dimensional function (Kotsiubivska, & Tymoshenko, 2019):

$$R: Z^2 \rightarrow R, R(i, j) = r_{ij}, \quad (2)$$

where $R(i, j)$ is the pixel value at position (i, j) , r_{ij} is the pixel intensity (e.g., reflectance, spectral brightness in a certain wavelength range, or another parameter).

The statistical analysis of the raster image begins with the calculation of its key characteristics, such as the average brightness value. The average brightness value for the entire raster image is calculated using the formula:

$$\mu = \frac{1}{N} \sum_{i=1}^M \sum_{j=1}^N r_{ij}, \quad (3)$$

where M and N correspond to the dimensions of the raster image (rows and columns, respectively), and the product $M \times N$ defines the total number of pixels in the image.

The average value defines the background of the image, enabling the identification of local deviations.

The standard deviation is determined using the formula:

$$\sigma = \sqrt{\frac{1}{N} \sum_{i=1}^M \sum_{j=1}^N (r_{ij} - \mu)^2}. \quad (4)$$

This parameter indicates the variability of brightness and is critical for the subsequent identification of anomalous zones.

Anomalous zones are identified using a statistical criterion based on deviations from the mean value to detect anomalous values in the case of a normal distribution of a random variable. This approach is widely used in the processing of satellite images and geospatial data analysis (Gavade, & Rajpurohit, 2021). According to this approach, values of the random variable that fall outside the range

$$\mu \pm k\sigma, \quad (5)$$

where μ is the expected value, σ is the standard deviation, and k is the anomaly coefficient, are considered potentially anomalous.

In this context, for raster data processing, this rule allows for the identification of areas where the intensity values significantly differ from the mean level, which may indicate the presence of natural or anthropogenic anomalies (Folini, Lenzi, & Biraghi, 2022). This method is based on the assumption of a Gaussian distribution of pixel intensity, which is typical for many natural phenomena and remote sensing of

the Earth (Hyttä et al., 2009). Thus, the determination of anomalous zones is described by the formula:

$$I_i = \mu + k\sigma. \tag{6}$$

This allows for the identification of regions where the values substantially exceed the background level. The approach relies on the assumption of a normal distribution of pixel intensities, which is typical for natural processes and satellite data.

Raster image binarization involves obtaining a mask $M(i,j)$, which is converted into a new raster file, where 1 corresponds to anomalous zones and 0 to the normal background:

$$M_{bin}(i,j) = \begin{cases} 255, & \text{if } M(i,j) = 1, \\ 0, & \text{if } M(i,j) = 0. \end{cases} \tag{7}$$

This mask allows for the visualization of anomalous areas and their storage in a standard format, such as GeoTIFF. At this stage, the projection and coordinate system of the input raster are assigned to the resulting mask.

Vectorization and Processing of Anomalous Zones

The process of vectorizing anomalous zones in a raster image is based on the *gdal.Polygonize()* algorithm, a function in the GDAL library that converts pixel regions with identical values into a set of closed polygons. Mathematically, this process can be represented as the construction of the set

$$P = \{A_i\}_{i=1}^N, \tag{8}$$

where A_i denotes individual regions formed by connected pixels with the same intensity value, and N represents the total number of identified anomalous zones.

Vectorization allows the conversion of a discrete representation of spatial data into a more suitable form for further analysis, ensuring effective processing and storage of information in geospatial vector formats such as Shapefile or GeoJSON.

The vectorization algorithm consists of several key stages. The first stage employs a scan-line algorithm, which identifies the boundaries of anomalous objects through the sequential scanning of the raster image. Next, the connected components of each object are determined and grouped into closed contours based on the topological properties of pixel connections. The final stage involves saving the resulting contours in vector form, enabling further spatial analysis, such as the calculation of geometric characteristics, the determination of the area and perimeter of anomalous zones, and integration with other geospatial data. This approach ensures high analysis accuracy and enables the automation of the anomaly identification process in satellite images and other geospatial data.

Upon completion of the polygonization stage, the obtained vector objects undergo filtering to eliminate

potential artifacts or noise that may have been generated during the analysis. The primary criterion for identifying such artifacts is the area of the polygon, which is determined using Gauss's formula (Gavade, & Rajpurohit, 2021):

$$S_i = \frac{1}{2} \left| \sum_{j=1}^n (x_j y_{j+1} - x_{j+1} y_j) \right|, \tag{9}$$

where S_i is the area of the polygon, x_j, y_j are the coordinates of its vertices, and n is the number of vertices of the polygon.

Among all identified anomalous zones, the polygon with the largest area is selected, as it is most likely to be an artifact or noise formation. If its area significantly exceeds the average area of other objects, it is removed from further analysis. The remaining polygons are preserved for further processing and interpretation, enhancing the accuracy and reliability of the geospatial analysis results.

The final step is to save the resulting vector objects as a new layer in Shapefile format.

Temporary File Management

During the operation of the plugin, temporary files are automatically created and managed, including the generation of directories for storing intermediate raster and vector data. This process may increase memory load and impact data processing performance. To ensure optimal use of system resources, all temporary files are automatically deleted either after their utilization is complete or upon the closure of QGIS. This approach helps prevent the accumulation of redundant data, enhances disk space efficiency, and minimizes memory usage, which is particularly critical when processing large volumes of geospatial data.

The aforementioned data processing sequence on the system side relies on active modules for raster and vector data that are executed each time user-defined parameters are modified (Fig. 3). These parameters include the selection of the raster layer and the specification of a sensitivity threshold (Jain, Duijn, & Mao, 2000). The defined sensitivity threshold determines the subset of data that satisfies the following expression:

$$\left| \frac{raster_{array} - \mu}{\sigma} \right| > \theta, \tag{10}$$

where the expression considers only positive values, as the modulus (interpreted by the system as the *abs* function) denotes the absolute value function. Here, *raster_{array}* refers to the data matrix, μ is the mean of the matrix, σ is the standard deviation, and θ is the sensitivity coefficient (threshold). The computed results are immediately made available to the user in the form of polygons representing anomalous values within the data array.

Thus, each change in user parameters triggers a processing cycle of raster and vector modules in sequence, enabling the visual evaluation of anomalous values based on the specified threshold.



Fig. 3. Schematic representation of the sequence of processes executed on the system side

Results

The results produced by the developed plugin (Fig. 4) were analyzed based on three types of satellite imagery: InSAR images for detecting vertical surface displacements, thermal infrared (TIR) images for determining land surface temperature (LST), and multispectral images in the green and near-infrared (NIR) spectral bands used to calculate the

Normalized Difference Water Index (NDWI). The automated analysis of these imagery types using the plugin significantly simplifies the interpretation of spatial data, thereby enhancing research efficiency and supporting timely decision-making in the fields of environmental monitoring and land management.

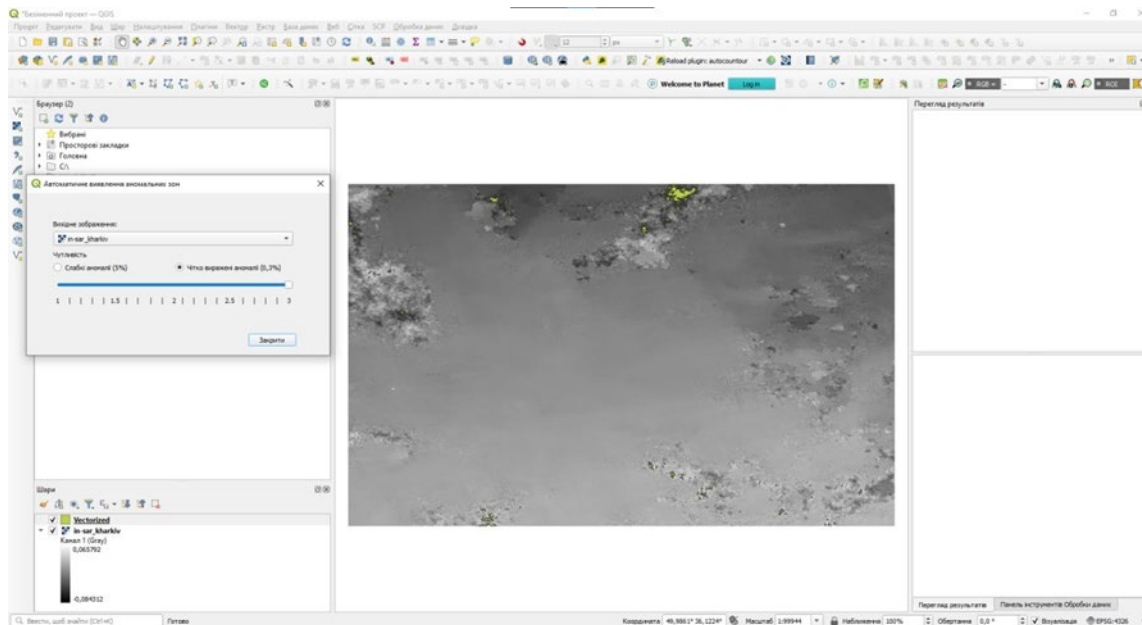


Fig. 4. General view of the developed plugin in QGIS software

Case 1: InSAR Imagery Analysis

The modern development of engineering infrastructure and urban areas is accompanied by substantial anthropogenic pressure on the Earth's surface. Construction of bridges, dams, underground utilities, and high-rise structures disturbs the natural equilibrium, potentially leading to vertical displacements of the Earth's crust, localized deformations, or even catastrophic failures (Krill, 2017). Accordingly, monitoring such processes is critically important for ensuring infrastructure safety and sustainable development.

The analysis of Sentinel-1 satellite imagery using the Differential Interferometric Synthetic Aperture Radar (D-InSAR) method serves as a powerful tool for detecting vertical surface displacements, particularly in urbanized environments (Minh, Hanssen, & Rocca, 2020). This method enables the detection of even minor topographic changes with high precision, making it indispensable for assessing geodynamic processes, risk forecasting, and informed decision-making in urban planning and engineering geology. The application of D-InSAR is especially relevant in zones of active construction, seismically hazardous areas, regions of underground resource extraction, and locations prone to subsidence or landslides (Kruglov, Hudak, & Kruhlov, 2025). The use of Sentinel-1 radar imagery facilitates the observation of displacement dynamics over time and the identification of long-term deformation trends.

In this case, the plugin was supplied with an InSAR satellite image of the city of Kharkiv (Fig. 5a), processed using the D-InSAR technique. After processing, the plugin automatically identified anomalous values indicating the presence of surface changes within the study area. These anomalies may correspond to vertical crustal deformations caused by either natural or anthropogenic factors. The resulting output provides a visualization of elevation

changes, enabling detailed examination of geodynamic processes in the region and further analysis of zones exhibiting anomalous displacements (Fig. 5b). The statistical characteristics derived from the processed InSAR imagery demonstrate significant variability in surface displacement values (Table 1). The largest anomalous area (polygon ID 193) shows a minimum displacement of -0.11 m, a maximum of -0.05 m, and an average of -0.07 m. Such negative values may indicate ground subsidence. Other significant polygons, such as ID 205 and ID 400, exhibit similar average values, pointing to the existence of subsiding areas in the region. The range of values in most cases does not exceed 0.03 m, indicating the localized nature of the detected changes.

Displacements with positive values (e.g., polygons ID 799, 632, and 596) indicate uplift of the Earth's surface. For instance, polygon ID 632 demonstrates a minimum value of 0.05 m, a maximum of 0.08 m, and a mean value of 0.05 m. Such values may reflect specific geodynamic processes, including ground uplift or deformation driven by anthropogenic or natural factors. In all cases, the standard deviation remains relatively low (0.01 – 0.004 m), confirming the uniformity of changes within each identified polygon. Overall, the resulting characteristics allow for a quantitative assessment of the extent of surface changes and facilitate the identification of zones requiring continued monitoring.

Thus, the automation of D-InSAR data analysis within QGIS significantly enhances the efficiency of deformation monitoring while ensuring a more objective, reproducible, and scalable approach to assessing geodynamic processes across various territories. This enables timely detection of potentially hazardous zones, which is especially important for areas undergoing intensive urban development or those with complex engineering and geological conditions.

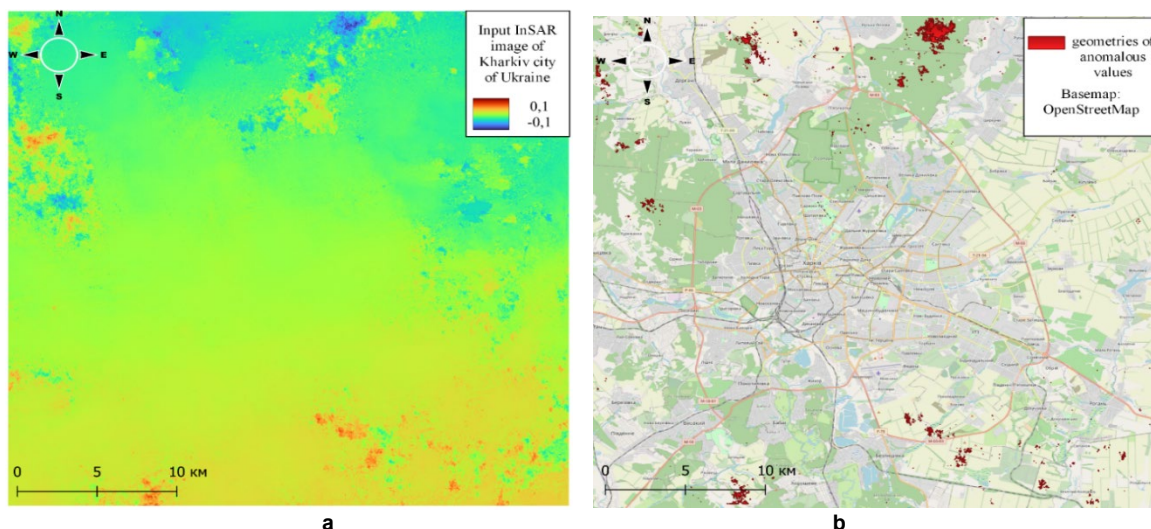


Fig. 5. Input image processed using the D-InSAR method (a); detected anomalous zones of vertical displacement (b)

Table 1

Polygon ID	Area, m ²	Min	Max	Mean	Standart deviation	Range	Sum of squares
193	1536244	-0,11	-0,05	-0,07	0,01	0,05	1,87
205	169109	-0,09	-0,05	-0,07	0,01	0,03	0,1
799	147380	0,05	0,07	0,05	0,01	0,03	0,08
400	131831	-0,08	-0,05	-0,07	0,01	0,03	0,09
632	93853	0,05	0,08	0,05	0,01	0,03	0,05
82	66415	-0,08	-0,05	-0,06	0,01	0,03	0,03
369	60226	-0,09	-0,05	-0,07	0,01	0,03	0,07
596	59012	0,05	0,08	0,06	0,01	0,03	0,05
308	49301	-0,08	-0,05	-0,06	0,004	0,02	0,02
840	42160	0,05	0,07	0,06	0,01	0,03	0,02
269	41401	-0,08	-0,05	-0,06	0,004	0,02	0,02
506	40645	-0,08	-0,05	-0,06	0,004	0,02	0,01

Case 2: Landsat 8/9 (Thermal Infrared Sensor)

Satellite imagery acquired via the Thermal Infrared Sensor (TIRS) onboard Landsat 8/9 satellites serves as a critical data source for monitoring temperature variations on the Earth's surface. This is particularly relevant in the context of climate change, as such data enable the identification of warming trends, overheating in urbanized areas, and fluctuations in soil moisture (Lischenko, Pazynych, & Filipovych, 2017; Filipovych, & Shevchuk, 2018).

Thermal sensor data, especially from TIRS, are employed for the monitoring of geothermal resources, detection of elevated temperatures in zones of volcanic activity, and analysis of terrain changes related to geological displacements and ground deformation. Furthermore, these data are valuable for assessing the ecological state of landscapes – particularly in areas affected by mining – where surface temperature shifts may indicate land degradation. Thermal imagery is also instrumental in detecting and forecasting exogenous processes such as erosion or landslides, as well as in evaluating anthropogenic impacts and pollution caused by human activities (Vivaldi et al., 2022). Additionally, thermal data contribute to climate change modeling and the analysis of urbanization effects, especially in detecting urban heat islands.

The analysis of Land Surface Temperature (LST) using the developed plugin includes the application of criteria for detecting minor anomalies, comprising no more than 5 % of the total dataset. The input image (Fig. 6a) is an atmospherically corrected Landsat product representing LST in degrees Celsius for the year 2020. The study area is located in the central part of Kyiv Oblast and is characterized by extensive agricultural land use, which has a notable environmental impact on

surrounding ecosystems – particularly the Supiy River – and features a clearly defined urban heat island in the city of Yahotyn, Kyiv Oblast, Ukraine.

The input thermal image (Fig. 6a) has the following characteristics: maximum temperature of 32.79 °C, mean temperature of 23.08 °C, minimum temperature of 14.07 °C, temperature range of 18.72 °C, and a standard deviation of 3.37 °C. Based on these metrics, 182 anomalous polygons were identified, each containing values that meet the predefined anomaly criteria. In total, the number of pixels with anomalous values amounts to 21.62 out of 455.60 (4.75 %).

The analyzed image exhibits a distinct spatial heterogeneity in thermal conditions, reflecting the complex interaction of natural and anthropogenic factors. The maximum recorded temperature is 32.79°C, the minimum is 14.07 °C, and the mean value is 23.08 °C, with a temperature range of 18.72 °C and a standard deviation of 3.37 °C (Tab. 2). In total, 182 anomalous figures were identified, occupying 21.62 pixels out of 455.60, representing 4.75 % of the total image area. All anomalous areas were classified into two categories: low-temperature anomalies (ranging from 14.06 °C to 16.33 °C), primarily associated with reservoirs and water bodies, and high-temperature anomalies (ranging from 29.45 °C to 32.79 °C), typical for dry open surfaces such as farmland and urban areas.

This thermal segmentation is also evident in the detailed analysis of selected features: for example, ID 159 and 88 show average temperatures of 14.81 °C and 15.37 °C, respectively, characteristic of moist or aquatic surfaces, whereas areas such as ID 109, 160, and 139 display elevated mean values above 30 °C, corresponding to dry open territories or urban zones. The variation in

standard deviation within the range of 0.27–0.71 °C indicates differing levels of temperature uniformity across individual geospatial objects. Large spatial structures, such

as ID 159, exhibit stable temperature gradients, which are crucial for the comprehensive analysis of landscape thermal conditions (Fig. 6b).

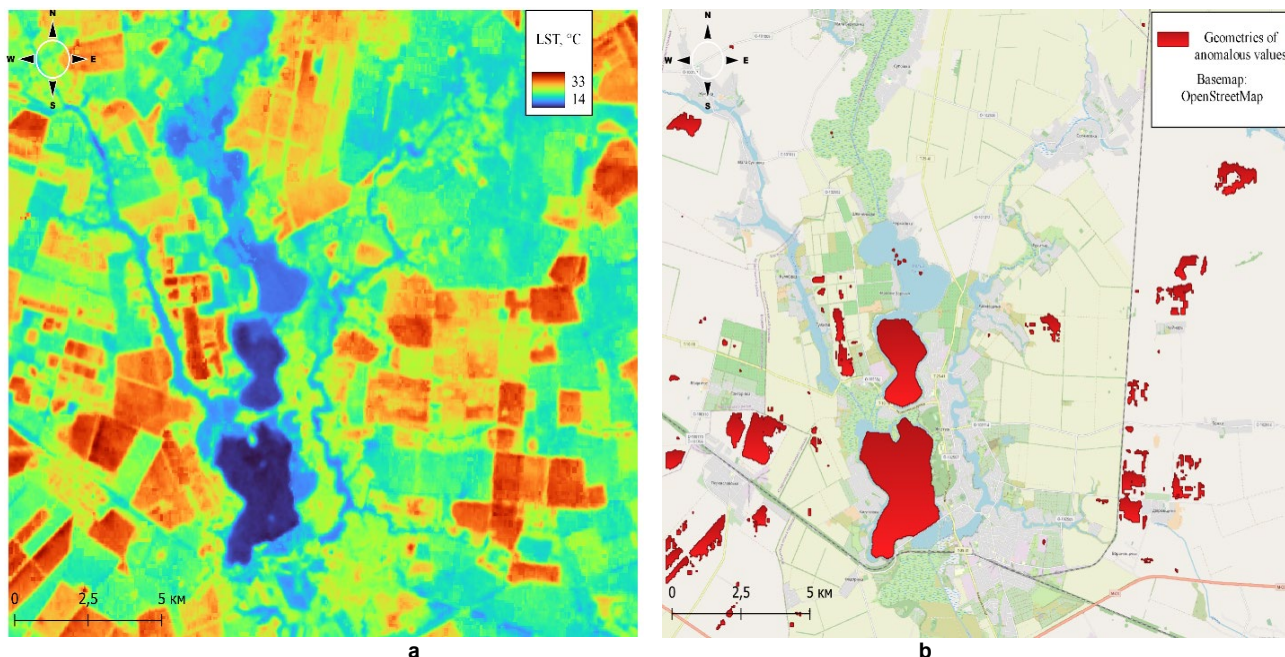


Fig. 6. Input LST image (a); detected anomalous zones of high and low temperature (b)

Table 2

Polygon ID	Area, m ²	Min	Max	Mean	Standart deviation	Range	Sum of squares
159	7453792	14,07	16,33	14,81	0,4	2,27	1344,38
88	3057343	14,49	16,33	15,37	0,38	1,85	492,43
109	1260731	29,83	32,79	30,76	0,65	2,96	581,46
26	683546	29,83	31,43	30,23	0,33	1,6	83,48
160	624957	29,83	32,47	30,68	0,71	2,64	345,52
17	454758	29,83	31,3	30,26	0,28	1,47	40,33
139	434077	29,83	31,96	30,5	0,44	2,13	93,28
102	433149	29,83	31,09	30,34	0,32	1,27	48
126	355727	29,83	31,21	30,25	0,35	1,38	48,54
79	329596	29,83	31,97	30,56	0,41	2,14	62,27
51	326010	29,83	31,49	30,24	0,38	1,66	50,99
113	285461	29,83	31,71	30,73	0,41	1,88	53,64

The application of the developed plugin significantly enhanced the efficiency of detecting geospatial objects with anomalous thermal characteristics based on user-defined criteria, thereby ensuring higher accuracy and timeliness in surface temperature monitoring. The obtained results can serve as a robust analytical foundation for forecasting climate trends, assessing ecological risks, and planning the rational use of land resources.

Case 3: Normalized Indices from Multispectral Imagery

As in the previously discussed cases, anomalous values help to identify the most affected zones characterized by specific index responses. In this instance, the Normalized Difference Water Index (NDWI) was used to detect surface water bodies (McFeeters, 1996); however, the use of other indices – such as NDVI, NDSI, NDDI, among others – can be beneficial for a wide range of thematic applications.

The area under investigation is located near the city of Yahotyn in Kyiv Oblast (Fig. 7a), along the Supiy River (Ukraine), which is known to experience periodic suffosion-induced subsidence (Marhes, 2024). The study of such

physical processes in this region is of high relevance, as they are widespread on the left bank of the Dnipro River and exert a negative impact on agricultural productivity. NDWI was specifically selected due to its sensitivity to moisture accumulation in microdepressions formed by subsidence (Trofyomenko et al., 2024).

NDWI values were derived from a PlanetScope satellite image (Planet Team, 2025), revealing predominantly dry or minimally moist areas with only limited evidence of water presence. Using the developed plugin, it was possible to visualize local terrain depressions – particularly bowl-shaped formations – where moisture accumulation was detected (Fig. 7b). In some instances, weakly expressed forms of linear erosion were also observed, further indicating irregularities in the surface hydrological regime. NDWI, which is responsive to the moisture content of vegetation and open water bodies, yielded uniformly negative values across the sample, ranging from -0.72 to -0.37. This confirms the predominance of dry soils or vegetation lacking free surface water.

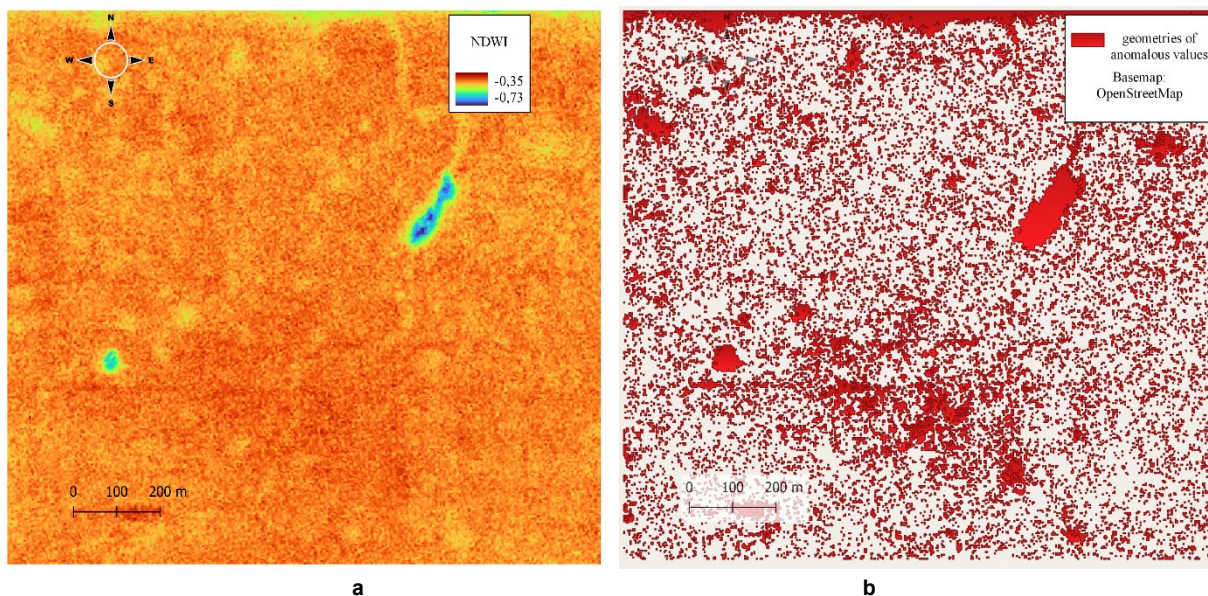


Fig. 7. Input NDWI image (a); Detected anomalous (critical) zones in the image (b)

Analysis of the statistical data (Table 3) reveals a degree of heterogeneity across the studied areas. The largest zone is represented by object ID 580, covering 35,057 pixels, with an average NDWI value of -0.5 and a relatively narrow range (0.2), indicating a relatively homogeneous moisture condition. In contrast, object ID 4294 is characterized by the highest standard deviation (0.07) and a broader range

(0.31), likely due to the presence of varying surface types or local hydrological contrasts. Other zones, particularly those with an area below 2,500 pixels (e.g., ID 6228), display stable NDWI values with minimal dispersion, which is typical for small, homogeneous micro-landscapes. The dominance of negative NDWI values across the dataset further confirms the prevalence of arid or low-moisture microenvironments.

Table 3

Polygon ID	Area, m ²	Min	Max	Mean	Standart deviation	Range	Sum of squares
580	35057	-0,6	-0,41	-0,5	0,02	0,2	1,3
4294	15426	-0,72	-0,42	-0,54	0,07	0,31	7,47
7362	4007	-0,43	-0,38	-0,41	0,01	0,05	0,05
2375	3836	-0,54	-0,43	-0,49	0,01	0,11	0,08
2636	3710	-0,55	-0,42	-0,49	0,01	0,13	0,06
6457	3071	-0,64	-0,47	-0,53	0,05	0,17	0,8
7820	2756	-0,43	-0,39	-0,42	0,01	0,04	0,03
7170	2630	-0,43	-0,39	-0,42	0,01	0,04	0,02
8608	2467	-0,43	-0,39	-0,42	0,01	0,04	0,02
6217	2062	-0,43	-0,38	-0,42	0,01	0,05	0,02
8962	2044	-0,43	-0,37	-0,41	0,01	0,06	0,03
6228	2008	-0,48	-0,39	-0,42	0,01	0,09	0,02

The statistical analysis of NDWI values indicates an overall low moisture content throughout the entire study area. These data may be used to identify drought-prone zones, track seasonal fluctuations in moisture regimes, or compare with other indices such as NDVI or NDBI. The most analytically valuable areas are those exhibiting high variability, which may serve as indicators of local environmental changes or anthropogenic impacts.

Discussion and conclusions

The development of effective methods for analyzing satellite imagery represents a key challenge in monitoring both natural and anthropogenic environmental changes. The proposed approach to automated anomaly detection is grounded in the application of statistical methods, enabling high accuracy and processing speed.

Traditional approaches to image analysis typically rely on visual interpretation and manual digitization of anomalous zones. However, this method is time-consuming, particularly when dealing with large datasets containing numerous anomalies. Manual identification becomes increasingly difficult over extensive or densely built-up areas. Moreover,

the results of such analysis often depend on the researcher's expertise and subjective interpretation, introducing potential error. The lack of a standardized algorithm further complicates reproducibility, which is critical for long-term environmental monitoring. Visual methods also fall short in handling large volumes of spatial data and accounting for spatial deformation patterns.

Given these limitations, the development of a plugin for QGIS that automates the identification of anomalous displacement zones is a timely and relevant solution. Automation allows for the standardization of analytical procedures, increased anomaly detection accuracy, and significant time savings. The integration of machine learning algorithms and geostatistical methods within the plugin enhances the precision of anomaly recognition and helps reduce data noise. Moreover, coupling the plugin with other geoinformation modules facilitates comprehensive analysis of interactions between surface deformations and influencing factors such as hydrogeological conditions and anthropogenic pressure.

The developed QGIS plugin streamlines satellite image analysis and greatly simplifies the identification of anomalous

zones. Its core functionality includes the use of threshold and statistical analysis methods to detect changes in geospatial data, contributing to more objective assessments and standardized outcomes. In addition, the plugin supports various types of satellite imagery – including InSAR, thermal infrared, and normalized index data – making it a versatile tool for a broad spectrum of researchers.

The algorithmic implementation is based on Python libraries such as NumPy, SciPy, and GDAL, which enable complex analytical computations to be seamlessly integrated into the QGIS environment. The use of thresholding and standard deviation calculations permits adaptive parameter tuning for anomaly detection, thereby reducing the likelihood of false positives.

Practical testing of the plugin has demonstrated its effectiveness in the context of automated surface change monitoring and hydrogeological assessment. Thanks to its intuitive graphical interface, users can easily configure analysis parameters and obtain results in the form of vector data, ready for further processing.

The testing process also generated ideas for future improvements. In particular, it was suggested to implement separate processing of positive and negative index or displacement values. This approach allows for consideration of the differing nature of physical processes or phenomena that produce anomalies of opposite signs – for example, ground subsidence versus surface uplift caused by anthropogenic or natural factors. Segregating these zones would enhance the accuracy of interpretation and improve decision-making based on the analytical results.

In summary, the developed plugin is an efficient tool for remote sensing research. It reduces the time required for satellite image analysis, increases accuracy, and standardizes approaches to environmental change assessment. Its integration into QGIS opens new avenues for geoinformation analysis, representing a promising direction for advancing monitoring methods for both natural and anthropogenic processes.

Authors' contribution: Vasyl Hudak – methodology, writing (review and editing), databases and data analysis, methodology; Serhii Marhes – conceptualization, data validation, graphic materials, writing (original draft); Vitalii Zatserkovnyi – formal analysis, revising of the manuscript, Mauro De Donatis – revision and editing.

Sources of funding. This research was conducted within the framework of the state-funded project "Integrated Models and Forecasting of Natural and Military Geohazards and Assessment of Their Impact on Critical Infrastructure" (State Registration No. 25BP049-01(M)).

References

- Cleveland, W. S. (1993). *Visualizing data*. Hobart Press. <https://www.hobartpress.com/visualizing-data>
- Filipovych, V., & Shevchuk, R. (2018). *Satellite technology for determining the heat load on the city in summer and ways to overcome it through green planning*. [Preprint]. <https://doi.org/10.13140/RG.2.2.17113.08807>
- Folini, A., Lenzi, E., & Biraghi, C. A. (2022). Cluster analysis: A comprehensive and versatile QGIS plugin for pattern recognition in geospatial data. *International Archives of Photogrammetry, Remote Sensing and Spatial Information Sciences*, XLVIII-4/W1-2022, 151–157. <https://doi.org/10.5194/isprs-archives-XLVIII-4-W1-2022-151-2022>
- Gavade, A. B., & Rajpurohit, V. S. (2021). Systematic analysis of satellite image-based land cover classification techniques: literature review and challenges. *International Journal of Computers and Applications*, 43(6), 514–523. <https://doi.org/10.1080/1206212X.2019.1573946>

Hyta, P. C., Hardie, R. C., Eismann, M. T., & Meola, J. (2009). Anomaly detection in hyperspectral imagery: Comparison of methods using diurnal and seasonal data. *Journal of Applied Remote Sensing*, 3(1), 033546.

Ivanik, O., Menshov, O., Bondar, K., Vyzhva, S., Khomenko, R., Hadiatska, K., Kravchenko, D., & Tustanovska, L. (2022). Integrated approach to modelling and assessing the landslide hazards at the regional and local scale in Kyiv urbanized area, Ukraine. *Modeling Earth Systems and Environment*. <https://doi.org/10.1007/s40808-022-01447-x>

Jain, A., Duin, R., & Mao, J. (2000). Statistical pattern recognition: A review. *IEEE Transactions on Pattern Analysis and Machine Intelligence*, 22(1), 4–37. <https://doi.org/10.1109/34.824819>

Janz, A., Jakimow, B., van der Linden, S., Thiel, F., & Dierkes, H. (2021). AVHYAS: A free and open-source QGIS plugin for advanced hyperspectral image analysis. In *2021 International Conference on Emerging Techniques in Computational Intelligence (ICETCI)*. IEEE. <https://doi.org/10.1109/ICETCI51973.2021.9574057>

Kotsiubivska, K., & Tymoshenko, V. (2019). Mathematical methods of image processing. *Digital Platform Information Technologies in Sociocultural Sphere*, 2(1), 41–54. [in Ukrainian]. [Кощюбівська, К., & Тимошенко, В. (2019). Математичні методи обробки зображень. *Цифрова платформа. Інформаційні технології в соціокультурній сфері*, 2(1), 41–54]. <https://doi.org/10.31866/2617-796x.2.1.2019.175653>

Kril, T. (2017). Causes of some hazardous engineering geological processes on urban territories. In *E3S Web of Conferences* (Vol. 24). EDP Sciences. <https://doi.org/10.1051/e3sconf/20172401009>

Kruglov, O., Hudak, V., & Kruhlov, B. (2025, April). *Exploring D-InSAR Technology for Monitoring Soil Erosion: Case Study in Kharkiv Region*. Paper presented at the 18th International Conference Monitoring of Geological Processes and Ecological Condition of the Environment, European Association of Geoscientists & Engineers.

Lisichenko, L., Pazynych, N., & Filipovych, V. (2017). Satellite monitoring of landslide development in the Pridnieprovsk zone of Kyiv. *Ukrainian Journal of Remote Sensing*, 15, 111–120 [in Ukrainian]. [Ліщенко, Л., Пазинич, Н., & Філіпович, В. (2017). Супутниковий моніторинг розвитку зсувів у Придніпровській зоні м. Києва. *Український журнал дистанційного зондування*, 15, 111–120]. <https://doi.org/10.36023/ujrs.2017.15.111>

Marhes, S. (2024). Satellite geoeological analysis of the peat-swamp system of the Supii River. *Ideas and Innovations in Earth Sciences*, 24, 74–75. <https://doi.org/10.30836/igs.ies.2024.34>

Marhes, S. (2025). *Autocountour QGIS Plugin* (Version 1.0) [Computer software]. GitHub. https://github.com/rnrhs/autocountour_qgis_plugin

MASAI Project. (n.d.). *MASAI: Pioneering damage assessment through AI and satellite technology*. Retrieved July 8, 2025, from <https://masai-project.eu/masai-pioneering-damage-assessment-through-ai-and-satellite-technology/>

McFeeters, S. K. (1996). The use of the Normalized Difference Water Index (NDWI) in the delineation of open water features. *International Journal of Remote Sensing*, 17(7), 1425–1432. <https://doi.org/10.1080/01431169608948714>

Meng, C., Wang, Y., Zhang, X., Mandal, A., Zhong, W., & Ma, P. (2017). Effective statistical methods for big data analytics. In *Handbook of research on applied cybernetics and systems science* (pp. 280–299). IGI Global.

Minh, D. H. T., Hanssen, R., & Rocca, F. (2020). Radar interferometry: 20 years of development in time series techniques and future perspectives. *Remote Sensing*, 12(9), 1364. <https://doi.org/10.3390/rs12091364>

Planet Team. (2025). *PlanetScope NDWI image 20241024_090954_85_250a_3B_AnalyticMS_SR_8b_harmonized_clip*. Planet Labs PBC. <https://www.planet.com/nextgenplanetoscope/>

QGIS Project. (2024). *Fetching plugins*. QGIS Documentation. https://docs.qgis.org/3.40/en/docs/training_manual/qgis_plugins/ fetching_plugins.html

Tempa, K., & Aryal, K. R. (2022). Semi-automatic classification for rapid delineation of the geohazard-prone areas using Sentinel-2 satellite imagery. *SN Applied Sciences*, 4(1), 141. <https://doi.org/10.1007/s42452-022-05028-6>

Trofymenko, P., Tomchenko, O., Poralo, R., Zatserkovnyi, V., & Stakhiv, I. (2024). Remote identification of micro-depression relief forms and soil cover areas of agro-landscapes in the Polissya region of Ukraine with signs of hydromorphism. *Bulletin of Taras Shevchenko National University of Kyiv. Geology*, 1(104), 98–106. <https://doi.org/10.17721/1728-2713.104.12>

Vivaldi, V., Bordoni, M., Mineo, S., Crozi, M., Pappalardo, G., & Meisina, C. (2022). Airborne combined photogrammetry–infrared thermography applied to landslide remote monitoring. *Landslides*, 20(2), 547–560. <https://doi.org/10.1007/s10346-022-01970-z>

Zhukov, M. N. (2008). *Mathematical statistics and processing of geological data*. Vyshcha Shkola [in Ukrainian]. [Жуков, М. Н. (2008). *Математична статистика та обробка геологічних даних*. Вища школа].

Отримано редакцію журналу / Received: 26.02.25

Прорецензовано / Revised: 19.03.25

Схвалено до друку / Accepted: 30.06.25